Computer Modeling of a Vertical Array in a Stratified Ocean

by

Lin Li

B. S., B. S., University of Science and Technology of China (1988)

M. S., University of Science and Technology of Beijing (1991)

Submitted in partial fulfillment of the
requirements for the degree of

Master of Science

at the

MASSACHUSETTS INSTITUTE OF TECHNOLOGY

and the

WOODS HOLE OCEANOGRAPHIC INSTITUTION

June 1994

Signature of Author .....

Joint Program in Oceanography/Applied Ocean Science and Engineering
Massachusetts Institute of Technology
Woods Hole Oceanographic Institution

Certified by ..

Ralph A. Stephen
Senior Scientist, Woods Hole Oceanographic Institution
Thesis Supervisor

Accepted by .

Marcia K. McNutt
Chair, Joint Committee for Geology and Geophysics
Massachusetts Institute of Technology
Woods Hole Oceanographic Institution
Joint Program in Oceanography/Applied Ocean Science and Engineering

Computer Modeling of a Vertical Array in a Stratified Ocean

by

Lin Li

Submitted to the Massachusetts Institute of Technology/
Woods Hole Oceanographic Institution
Joint Program in Oceanography/Applied Ocean Science and Engineering
on May 6, 1994 in partial fulfillment of the
requirements for the degree of

Master of Science in Oceanography

Abstract

The response of vertical arrays at single frequencies (CW) and for homogeneous media is well known. This paper addresses the issues of frequency dependence and sound velocity gradients for the vertical array response in a deep ocean. I have modified the synthetic seismogram code of Neil Frazer, Subhashis Mallick and Dennis Lindwall to address this problem. The code uses a rearrangement of the Kennett reflectivity algorithm (Kennett, 1974, 1983) which computes the geoacoustic response for depth dependent media and pulse sources by the wave number integration method. The generalized Filon method is applied to the slowness integral for an additional increase in speed (Frazer and Gettrust, 1984; Filon, 1928). The original code computes the response of a single source at a specified depth. The new code has several improvements over the previous one. First, it is a much simplified code addressing only acoustic interaction. The total length is about half the length of the original code. Secondly, the code can compute the response of a vertical array of point sources. By changing the phase delay between the sources, we can steer the beam to the places of most interest. Thirdly, the code reduces considerably numerical noise at large offsets. The original work has numerical noise beyond about 30 km offset at 50 Hz which limits the application of reflectivity modeling in long range problems. The improvement comes with the optimization of the program, both in the speed and program structure. The improved algorithm can be used to get the far offset response (up to 150 km) of a vertical array in the deep ocean at frequencies up to at least 250 Hz. The modeling results are compared to analytical and benchmark solutions. The modified reflectivity code can be applied to the study of pulsed-vertical array sources such as were deployed on the ARSRP (Acoustic Reverberation Special Research Program) acoustic cruises.

Thesis Supervisor: Ralph Stephen

Senior Scientist
Woods Hole Oceanographic Institution

Acknowledgments

This work was supported by the National Science Foundation under grant number OCE-91-18943, the Office of Naval Research under grant number N00014-90-J-1493 and Woods Hole Oceanographic Institution.

The successful completion of this thesis was made possible by the support and encouragement of my friends and colleagues. Special appreciation is given to,

- Ralph Stephen, my advisor, for his confidence, great guidance, patience and friendship. He always had time to talk with me and always with a positive attitude.
- Marcia McNutt, for her encouragement, suggestion and a lot of help.
- Dick Von Herzen, for his friendly encouragement, his advice both in science and way of life.
- Bob Detrick, for his help and encouragement.
- John Collins, for his help at the time I needed it most.
- Steve Swift, for his introduction and follow-on help in the project.
- Tom Bolmer, did a tremendous job keeping the computer running with good performance.
- Mom and Dad, who raised me to be tough, to be intelligent, to be anyone that I dream to be.
- Lu Zang, my wife, to whom the thesis is dedicated.

Special thanks also go to Emily Hooft, Javier, Cecily ... for their encouragement and help. Thanks God for giving me the strength and the luck to be with those nice people.

Contents

List of Figures

Chapter 1

Introduction

The ARSRP (Acoustic Reverberation Special Research Program) Reconnaissance Experiment was conducted from 25 July to 19 August 1991, and in 1993 the ARSRP acquired detailed geological and acoustic backscatter data from three sites in the ARSRP corridor in the western North Atlantic. A vertical line array (VLA) of 10 coherent sources was used, and its beam angle can be steered (Elliot, 1991). Specific long term objectives of these efforts are: 1) "to characterize the variations in bottom topography and sub-bottom properties that control the scattering of low frequency acoustic waves", 2) "to develop theoretical and numerical techniques capable of predicting the low frequency acoustic wavefield scattered from geologically realistic models of the bottom/sub-bottom environment", and 3) "to isolate from these scattering models the physical mechanisms which dominate the long-range reverberation from the seafloor."

The challenge for the ARSRP is to analyze the acoustic and geological data and to demonstrate a predictive modeling capability for low angle seafloor backscatter. In order to achieve such a goal, it is important to model the acoustic responses on the seafloor for the VLA. There are several interesting objectives in the numerical modeling: 1) what is the effect of the free surface on the sea floor response, 2) what is the effect of the ocean velocity gradient on the response, 3) how do the above factors affect CW and pulse sources, etc.

Ray theory and parabolic equation methods (Smith and Tappert, 1993) are com-

mon in ocean acoustics to compute the acoustic field. They are compared in Tolstoy et al. (1985). Özlüer (1992) studied the refraction effects on vertical line array beamforming applying a simple ray theory method. She studied the responses from 10 omnidirectional point sources with linear phase tapering equivalent to a steering of 6 deg depression. There are big inaccuracies involved in the results after 30 km horizontal offset.

In order to study the vertical array interference problem more completely and to get a more accurate picture of the interference response in the deep ocean for a wide variety of outgoing beam angles from the vertical array, we use the reflectivity modeling method. The reflectivity method has been widely used to compute synthetic seismograms in layered media. In fact, it has contributed to a better understanding of the earth's structure, both on the continents and beneath the ocean (for example, Braille and Smith (1975), Spudich and Orcutt (1980a, b), and Kempner and Gettrust (1982a,b)).

Its main advantage is its capacity to compute a total solution of the wave field for a given model. A matrix method is generally used to compute the response of the model in frequency-wavenumber space. This includes contributions from all possible generalized rays within the reflecting zone (Kennett 1974, 1983; Kind, 1976). The original reflectivity version of Fuchs and Müller (1971) required the source and receiver to be above the reflecting zone, but the method was subsequently modified by Stephen (1977) to accommodate a receiver buried within the reflecting zone. In practice, there are some disadvantages of the reflectivity method. The main one is the usually long computation time required in the modeling. So, even though there has been extensive study of the theory of the reflectivity method, adequate care must be taken to implement the theory and also to balance the speed and accuracy. This is especially true for our vertical array problem which has multiple sources and which is required to compute long range responses in the deep ocean.

Chapter 2

Background

2.1 Reflectivity Method

The reflectivity method has long been used by seismologists for modeling both land and marine reflection and refraction data. The method, originally proposed by Fuchs and Müller(1971), was extensively modified by Kennett (1974). The calculations are done essentially in two steps:

- A reflectivity function $R(\omega, p)$ is calculated in the frequency-ray parameter (wavenumber) domain. This is performed by layer iteration starting from the free surface down to the deepest interface. In each step of the iteration, all orders of multiple-bounce paths in the layer are included. At the final step, one obtains a reflectivity function that includes all possible ray paths from the source to the receiver.

- The second step involves numerical evaluation of a double integral of the form

$$u(x,t) = \frac{1}{2\pi} \int d\omega \exp(-i\omega t) \times \int dp f(\omega, p) \exp[\sigma g(p)] \qquad (2.1)$$

  where $\sigma = i\omega x$ and $g(p) = p$.

The integration over frequency ω is usually carried out by a fast Fourier transform (FFT). A complex frequency with a constant imaginary part is used in the integral

to attenuate the wraparound caused by the use of the FFT.

The integrand of the integral over the ray parameter p is highly oscillatory and use of the trapezoidal rule would require a very small step size in p. Use of a generalized Filon method (GFM) (Frazer, 1978; Frazer and Gettrust, 1984) allows one to use a much larger step size in p. The sampling interval δp depends both on frequency and the maximum range needed for the calculation, i.e., long range and high-frequency calculations require a very small step size in p to avoid spatial aliasing.

The background and limitations of the method are described in the two papers of Mallick and Frazer (1987; 1988). We modified their program for our vertical array problem.

The compressional potential of the wave from an explosive point source is

$$\phi_0(r,z,t) = \frac{1}{R}F(t - \frac{R}{\alpha_1}) \tag{2.2}$$

where $R^2 = r^2 + z^2$. Its Fourier transform can be written in integral form

$$\overline{\phi}_0(r,z,\omega) = \overline{F}(\omega)\int_0^\infty \frac{k}{j\nu_1}J_0(kr)\exp(-j\nu_1 z)dk \tag{2.3}$$

where $\overline{F}(\omega)$ is the Fourier transform of the excitation function $F(t)$, $J_0(kr)$ the Bessel function of the first kind and order zero, j the imaginary unit, k the horizontal wave number, and

$$\nu_1 = (k_{\alpha_1}^2 - k^2)^{\frac{1}{2}} \tag{2.4}$$

is the vertical wave number ($k_{\alpha_1} = \omega/\alpha_1$).

Since we are mainly interested in the application of synthetic seismograms to explosion seismological studies, we can replace the Bessel functions by their asymptotic approximations for large arguments(Fuchs and Müller, 1971) , which is good for $kr > 14$ (Corresponding to a source with a frequency of 200 Hz, this approximation is good for ranges down to 16.7m. The synthetic seismograms based on this

approximation will be incorrect at normal incidence) :

$$J_0(x) \approx \sqrt{\frac{2}{\pi x}} \cos(x - \frac{\pi}{4}) = \frac{1}{\sqrt{2\pi x}} \left\{ \exp[j(x - \frac{\pi}{4})] + \exp[-j(x - \frac{\pi}{4})] \right\} \tag{2.5}$$

$$Y_0(x) \approx \sqrt{\frac{2}{\pi x}} \sin(x - \frac{\pi}{4}) = \frac{-j}{\sqrt{2\pi x}} \left\{ \exp[j(x - \frac{\pi}{4})] - \exp[-j(x - \frac{\pi}{4})] \right\} \tag{2.6}$$

Where J_0 and Y_0 are Bessel functions of first and second kind respectively and both are of order zero.

The second exponential term in the above equations corresponds to waves propagating in the positive r-direction (away from the source), whereas the first term describes waves traveling in the negative r-direction (towards the source).

2.2 The Reflectivity Function in a Layered Water Column

Fig. 2-1 shows the geometry and notation for the derivation of a layered half space. The pressure reflection and transmission coefficients at the boundary of layers 1 and 2 for a wave incident from above are:

$$\Re_{12}(\theta_1) = \frac{\rho_2 c_2 \cos\theta_1 - \rho_1 c_1 \cos\theta_2}{\rho_2 c_2 \cos\theta_1 + \rho_1 c_1 \cos\theta_2} \tag{2.7}$$

$$\Im_{12}(\theta_1) = \frac{2\rho_2 c_2 \cos\theta_1}{\rho_2 c_2 \cos\theta_1 + \rho_1 c_1 \cos\theta_2} \tag{2.8}$$

with similar expressions for $\Re_{23}$ and $\Im_{23}$. From Figure 2-1, the total up-traveling signal is the sum of an infinite number of partial transmissions and reflections. Each path within the layer has a phase delay $2k_2 h_2 \cos\theta_2$, where $k_2 \cos\theta_2$ is the vertical component of the wave number in the layer. By letting the incident signal have unit amplitude, the total reflection $\Re_{13}$ is

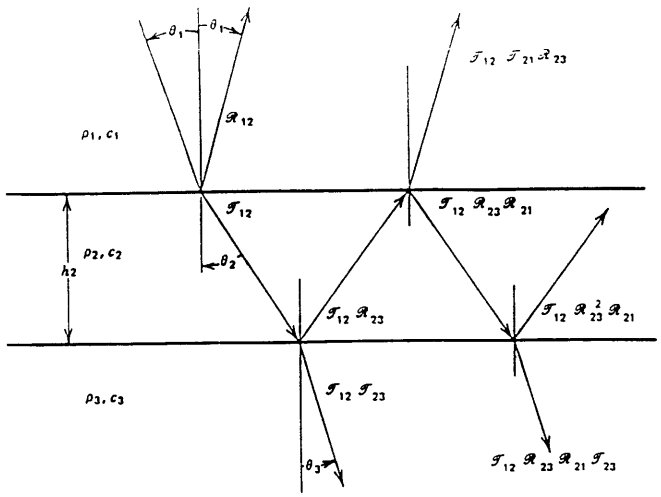

Figure 2-1: Reflection and transmission at a thin layer(From Figure 2.10.2. in Clay and Medwin, 1976)

$$\Re_{13}(\theta_1,\omega) = \Re_{12} + \Im_{12}\Im_{21}\Re_{23}\exp(-2i\Phi_2) + \Im_{12}\Im_{21}\Re_{23}{}^2\Re_{21}\exp(-4i\Phi_2) + \ldots \quad (2.9)$$

$$\Phi_2 = k_2 h_2 \cos\theta_2 \quad (2.10)$$

After $\Re_{12}$, terms in (2.9) have the form of a geometric series

$$S = \sum_{n=0}^{\infty} r^n = (1-r)^{-1} \quad for \quad r < 1$$

$$\Re_{13} = \Re_{12} + \Im_{12}\Im_{21}\Re_{23}\exp(-2i\Phi_2)\sum_{0}^{\infty}[\Re_{23}\Re_{21}\exp(-2i\Phi_2)]^n \quad (2.11)$$

Note that the reflection and transmission coefficients at a single interface are frequency independent (i.e. a function of angle or ray parameter only). When the propagation through a layer is considered (i.e. using Φ_2), the coefficients become frequency dependent.

We can reduce equation 2.11 by using the following relations, which come from equations 2.7 and 2.8,

$$\Re_{12} = -\Re_{21} \tag{2.12}$$

$$\Im_{12}\Im_{21} = 1 - \Re_{12}{}^2. \tag{2.13}$$

We have

$$\Re_{13} = \frac{\Re_{12} + \Re_{23}\exp(-2i\Phi_2)}{1 + \Re_{12}\Re_{23}\exp(-2i\Phi_2)}. \tag{2.14}$$

The transmission through the layer for a unit incident signal is

$$\Im_{13} = \Im_{12}\Im_{23}\exp(-i\Phi_2) + \Im_{12}\Im_{23}\Re_{23}\Re_{21}\exp(-3i\Phi_2) + \ldots \tag{2.15}$$

This is a geometric series, and the sum is

$$\Im_{13} = \frac{\Im_{12}\Im_{23}\exp(-i\Phi_2)}{1 + \Re_{12}\Re_{23}\exp(-2i\Phi_2)} \tag{2.16}$$

Both the $\Re_{13}$ and $\Im_{13}$ are oscillatory functions and depend on $\Phi_2 = k_2 h_2 \cos\theta_2$. They are functions of frequency and angle of incidence for a given layer.

We then can derive the total reflection and transmission of n layers, by repeated applications of the single layer coefficient.

As in Fig. 2-2 the reflection from the lower half space is $\Re_{(n-1)n}$. Applying equation 2.14 the reflection coefficient at the top of the $n-1$ layer is

$$\Re_{(n-1)n} = \frac{\Re_{(n-2)(n-1)} + \Re_{(n-1)n}\exp(-2i\Phi_{n-1})}{1 + \Re_{(n-2)(n-1)}\Re_{(n-1)n}\exp(-2i\Phi_{n-1})}. \tag{2.17}$$

We can repeat the above process to get $\Re(n-3)n$, the reflection coefficient for the layers beneath the interface, which is

$$\Re_{(n-3)n} = \frac{\Re_{(n-3)(n-2)} + \Re_{(n-2)n}\exp(-2i\Phi_{n-2})}{1 + \Re_{(n-3)(n-2)}\Re_{(n-2)n}\exp(-2i\Phi_{n-2})}. \tag{2.18}$$

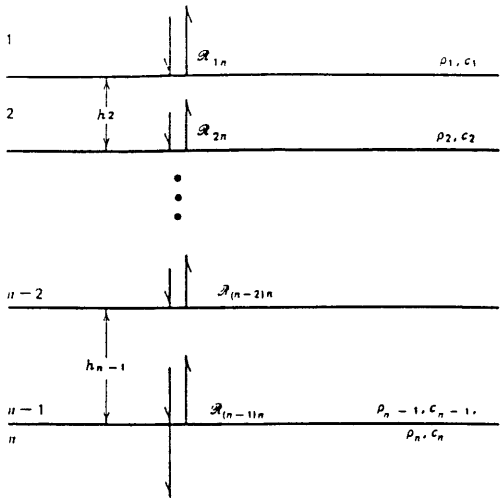

Figure 2-2: Reflection from a layered half space(From Figure 2.10.3. in Clay and Medwin, 1976)

Continuing the above calculation upward to the top, we have

$$\Re_{1n} = \frac{\Re_{12} + \Re_{2n}\exp(-2i\Phi_2)}{1 + \Re_{12}\Re_{2n}\exp(-2i\Phi_2)} \tag{2.19}$$

By letting the reflection coefficient $\Re_{1n}$ represent all the frequency and angle dependence, we simplify the expression for the reflection from a multiple layered half space. The above process can also be applied to get the transmission coefficient from a multiple layered half space. So, for large ranges, we can get the composite pressure reflection and transmission coefficients by applying the above layer iteration approach.

2.3 Computation of the Slowness Integral

In the reflectivity method, we do the numerical evaluation of the slowness integral, in the form

$$u(x,\omega) = \int_0^\infty \omega^2 p dp J_0(\omega p x)\tilde{u}(\omega,p) \tag{2.20}$$

where J_0 denotes the first kind Bessel function of order zero. This integral is oscillatory and in a normal integration scheme many steps are necessary in computing this when ωx is large. The step size used is inversely proportional to ωx. The program uses the generalized Filon method given by Frazer (1978) and Frazer and Gettrust (1984), which requires the step size to be inversely proportional to $(\omega x)^{1/2}$, which allows higher ωx response, for a given step size and a given error in computation.

To use the generalized Filon method, we transform the integral of equation 2.20 into (see Chapman 1978)

$$\int_\Gamma \frac{\omega^2}{2} p dp H_0^{(1)}(\omega p x)\tilde{u}(\omega,p) \tag{2.21}$$

where Γ is the contour of integration (shown in Fig. 2 of Frazer and Gettrust (1984)). The $H_0^{(1)}$ stands for a Hankel function of type 1 and order zero. The details for the transformation from equation 2.20 to equation 2.21 are shown by Chapman (1978).

We can rewrite equation 2.21 as

$$\int_\Gamma f(p) e^{Sg(p)} dp, \tag{2.22}$$

where

$$f(p) = \frac{\omega^2}{2} p H_0^{(1)}(\omega p x) e^{-i\omega p x}\tilde{u}(\omega,p)$$

$$S = i\omega x$$

and

$$g(p) = p$$

Application of the standard trapezoidal rule to the integral in equation 2.22, between the limits a and b, gives the quadrature formula

$$\int_a^b f(p)e^{Sg(p)} = \frac{1}{2}[f(a)e^{Sg(a)} + f(b)e^{Sg(b)}]\delta p \tag{2.23}$$

This formula does not work well because it assumes that $f(p)e^{Sg(p)}$ is well approximated by a linear function over the interval (a, b), while actually it is highly oscillating. If, we assume that both $f(p)$ and $g(p)$ are well approximated by different linear functions on (a, b), then we get the generalized Filon method analog of the trapezoidal rule (Frazer, 1978):

$$\int_a^b f(p)e^{Sg(p)}dp = \frac{\delta p}{2}[f(a)e^{Sg(a)} + f(b)e^{Sg(b)}], \quad for \quad \delta(g) = 0 \tag{2.24}$$

$$\int_a^b f(p)e^{Sg(p)}dp = \frac{\delta p}{S\delta(g)}[\delta(fe^{Sg}) - \frac{\delta(f)\delta(e^{Sg})}{S\delta(g)}], \quad otherwise \tag{2.25}$$

where, δp denotes $p_2 - p_1$, $\delta(g)$ denotes $g(p_2) - g(p_1)$, etc. It can be derived by replacing the integrand in the left-hand side of 2.23 by

$$[f_1 + (p - p_1)\frac{\delta(f)}{\delta(p)}]exp\left\{s[g_1 + (p - p_1)\frac{\delta(g)}{\delta(p)}]\right\}$$

The generalized Filon method greatly improves the quality of the synthetic result. It saves computation time by as much as 80 percent (Mallick and Frazer, 1987). A straightforward error analysis shows that, for a given accuracy, the step size in 2.23 is proportional to $|s|^{-1}$ whereas the step size to 2.25 is proportional to $|s|^{-1/2}$(Frazer and Gettrust, 1984).

The integral in equation 2.25 is simplified by letting $\delta p = \delta(g)$ and removing the term $\delta p/\delta(g)$:

$$\int_a^b f(p)e^{Sg(p)}dp = \frac{1}{S}[\delta(fe^{Sg}) - \frac{\delta(f)\delta(e^{Sg})}{S\delta(g)}], \quad otherwise \tag{2.26}$$

The results using equation 2.26 show great improvement in terms of the quality of the modeling result. Applying equation 2.25 as in the original program, there is

a big numerical noise problem beyond about 30km offset which limits the application of reflectivity modeling in long range problems. The optimized program using equation 2.26 reduces significantly the noise at large offsets. In the integral 2.25, the p and $g(p)$ are very small. This results in more numerical error than the simplified integral 2.26.

For the reflectivity method, we need to evaluate the integral:

$$u(\omega, x) = \int_0^{\infty - i_0} k dk \tilde{u}(\omega, k) J_n(kx) \tag{2.27}$$

in which J_n is the Bessel function of order n, and k is the wavenumber. Here advantage is taken of the relation (Olver, 1972, formula (9.2.19))

$$J_n = M_n \cos \theta_n \tag{2.28}$$

where the definitions of M_n and θ_n are:

$$M_n = \tan^{-1}(Y_n / J_n) \tag{2.29}$$

$$\theta_n = (J_n{}^2 + Y_n{}^2)^{\frac{1}{2}} \tag{2.30}$$

The functions M_n and θ_n are available as polynomial approximations (Allen, 1954; Ovler, 1972, formula (9.4.3) and (9.4.6)) for values of kx greater than three. For values of kx less than three, exact values of M_n and θ_n could be computed (Olver, 1972, formula (9.2.17)).

The asymptotic expansion of θ_n is (Olver, 1972, formula (9.2.29))

$$\theta_n = kx - \alpha_n + O(|kx|^{-1}) \tag{2.31}$$

where

$$\alpha_n = \frac{1}{4}(2n + 1)\pi$$

So, the equation 2.27 can be written as:

$$u(\omega, x) = \int_0^{\infty - i_0} dk f_1(k) e^{ixk} + \int_0^{\infty - i_0} dk f_2(k) e^{-ixk} \tag{2.32}$$

in which

$$f_1(k) = \frac{1}{2} k \tilde{u}(\omega, k) M_n e^{i(\theta_n - kx)} \tag{2.33}$$

$$f_2(k) = \frac{1}{2} k \tilde{u}(\omega, k) M_n e^{-i(\theta_n - kx)} \tag{2.34}$$

Equation 2.32 is exact, and yet the functions, f_1 and f_2, are relatively non-oscillatory because of 2.31. More importantly, each integral on the right-hand side of 2.32 is of the form 2.22, and so they can be evaluated using the generalized Filon integration method.

In the modeling of refraction data, x is usually greater than four or five wavelengths, and then the following simpler procedure can be applied. In equation 2.32 replace θ_n by $kx - \alpha_n$ and M_n by $(2/\pi kx)^{1/2}$ (Frazer, 1988).

The $u(\omega, x)$ can now be evaluated using the generalized Filon formula 2.26 with $g(p) = p$ and $s = i\omega x$.

Chapter 3

Theory of Vertical Array Interference for Harmonic Sources

3.1 Notation and Example Parameters

In our study, we use the following notation as shown in Fig. 3-1. We denote W as the total distance between the top source and the bottom source, d denotes the neighboring source distance, h is the depth of the top source from the free surface and ϕ is the grazing or dip angle of the ray to a receiver at a large distance from the array. Unless otherwise specified, all of the plotting will have the following parameters: $W = 5.49\lambda$, $h = 24.755\lambda$, which implies that the distance between the surface to the midpoint of the 10 sources is 27.5λ and the distance between the neighboring sources is 0.61λ. In the case of a frequency of $250Hz$ and a velocity of $1.5km/s$ (so that the wavelength $\lambda = 6m$), $d = 3.66m$ and $h + \frac{W}{2} = 165m$.

3.2 Dipole Interference

3.2.1 The Field from a Single Source

A sinusoidaly excited source expands and contracts repeatedly. The resulting contractions (density increases) and dilatations (density decreases) in the medium move

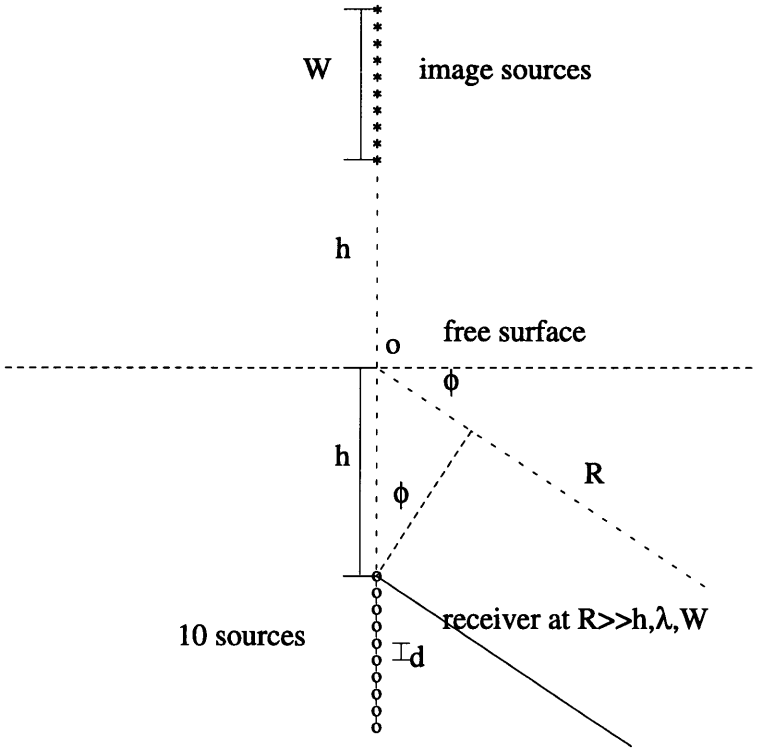

Figure 3-1: The Notation for Multiple Source Interference beneath a Free Surface

away from the source at the sound speed c, as would the disturbance from an impulsive source. This disturbance is called a continuous wave (CW), and it comes from a CW source. The distance between adjacent contractions along the direction of travel is the wavelength λ.

Assume that an omnidirectional CW sinusoidal point source in a homogeneous medium has the pressure at unit distance given by:

$$P = P_0 * \sin(\omega t) \tag{3.1}$$

So, at distance R, the pressure at a given time t will be:

$$P_r = \frac{P_0}{R} * \sin \omega(t - \tau) \tag{3.2}$$

where τ is the phase delay due to the travel time in the medium ($\tau = R/c$) and c is the wave velocity.

The field intensity (transmitted power per unit area), I, will be:

$$I = \frac{\overline{P^2}}{\rho c} = \frac{P_0^2}{2\rho c R^2} \tag{3.3}$$

where $\overline{P^2}$ is the ensemble average of P^2 in the time domain, ρ is the density of the medium and c is the wave speed in the medium.

3.2.2 The Field from Two Sources

Under the same assumption as the single source, two sources will generate an interference pattern.

The pressure at the receiver R is given by

$$P_r = P_1 + P_2 \tag{3.4}$$

where

$$P_1 = \frac{P_0}{R_1} * \sin\phi_1 = \frac{P_0}{R_1} * \sin\omega(t-\tau_1) \tag{3.5}$$

$$P_2 = \frac{P_0}{R_2} * \sin\phi_2 = \frac{P_0}{R_2} * \sin\omega[(t-\tau_2)+\delta_0] \tag{3.6}$$

(τ_1 and τ_2 are the wave travel time from source 1 and source 2 to the receiver respectively, δ_0 is the phase difference of the sources)

Then the field intensity will be:

$$I = \frac{\overline{P^2}}{\rho c} = \frac{\overline{(P_1+P_2)^2}}{\rho c} = \frac{\overline{P_1^2}}{\rho c} + \frac{\overline{P_2^2}}{\rho c} + \frac{2\overline{P_1P_2}}{\rho c} = I_1 + I_2 + \frac{2\overline{P_1P_2}}{\rho c} \tag{3.7}$$

(I_1 and I_2 are the intensity due to single sources in the absence of the other source, and the term $\frac{2\overline{P_1P_2}}{\rho c}$ corresponds to the interference of the two sources.)

At the same frequency, the phase shift ,δ, between waves from two adjacent sources is independent of time:

$$\delta = \phi_2 - \phi_1 = \omega(\tau_1 - \tau_2) + \delta_0 \tag{3.8}$$

$$= \frac{2\pi}{\lambda} * (r_1 - r_2) + \delta_0 \tag{3.9}$$

(λ is wave length, r_1 and r_2 are the distances from the two sources to the receiver respectively, and δ_0 is the phase delay of the top source relative to the bottom source).

Then

$$I = I_1 + I_2 + 2\sqrt{I_1 I_2}\cos\delta \tag{3.10}$$

Discussion:

- When $I_1 = I_2 = I_0$, which is the case when the two sources have the same intensity, we have $I = 4I_0\cos^2\frac{\delta}{2}$. For the case with $\delta = 0$, the phase shift offsets the phase difference due to the separation of the sources and we have $I = 4I_0$.

- Figures 3-2 and 3-3 show the interference between two sources at four typical separations of λ, $\lambda/2$,$\lambda/4$ and $\lambda/8$ with ($\delta_0 = 0$). From these plots, it can be seen that within one wavelength, as the distance of the sources decrease,

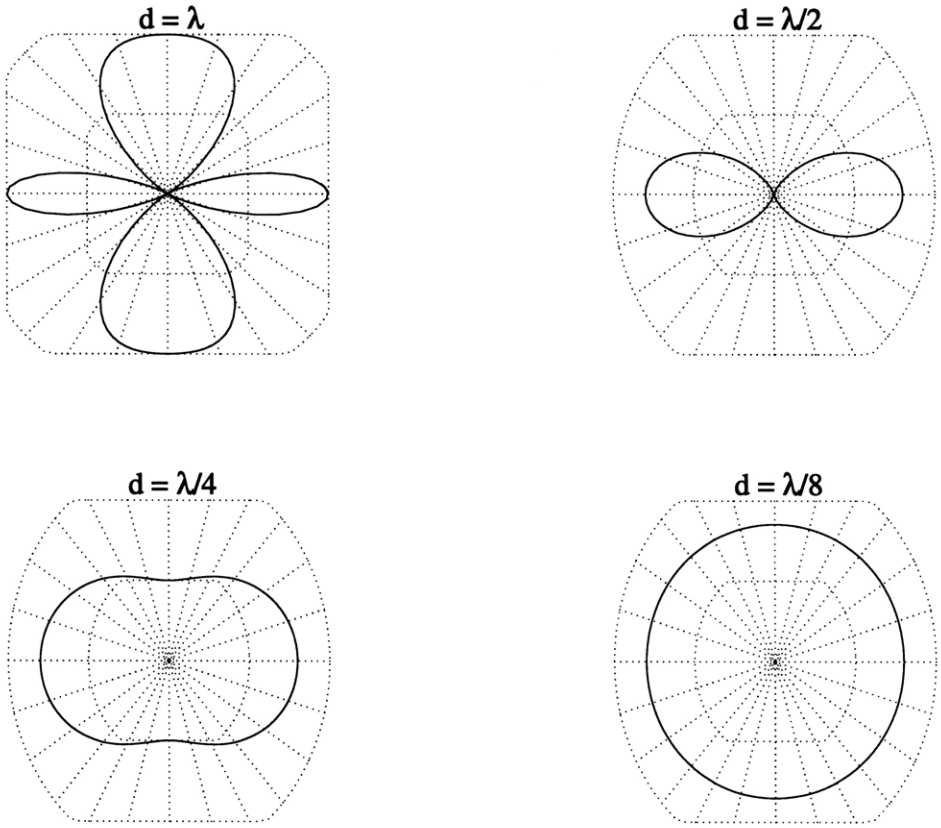

Figure 3-2: Interference Patterns for Two CW Sources without a Free Surface Plotted as Rose Diagrams, with zero phase shift

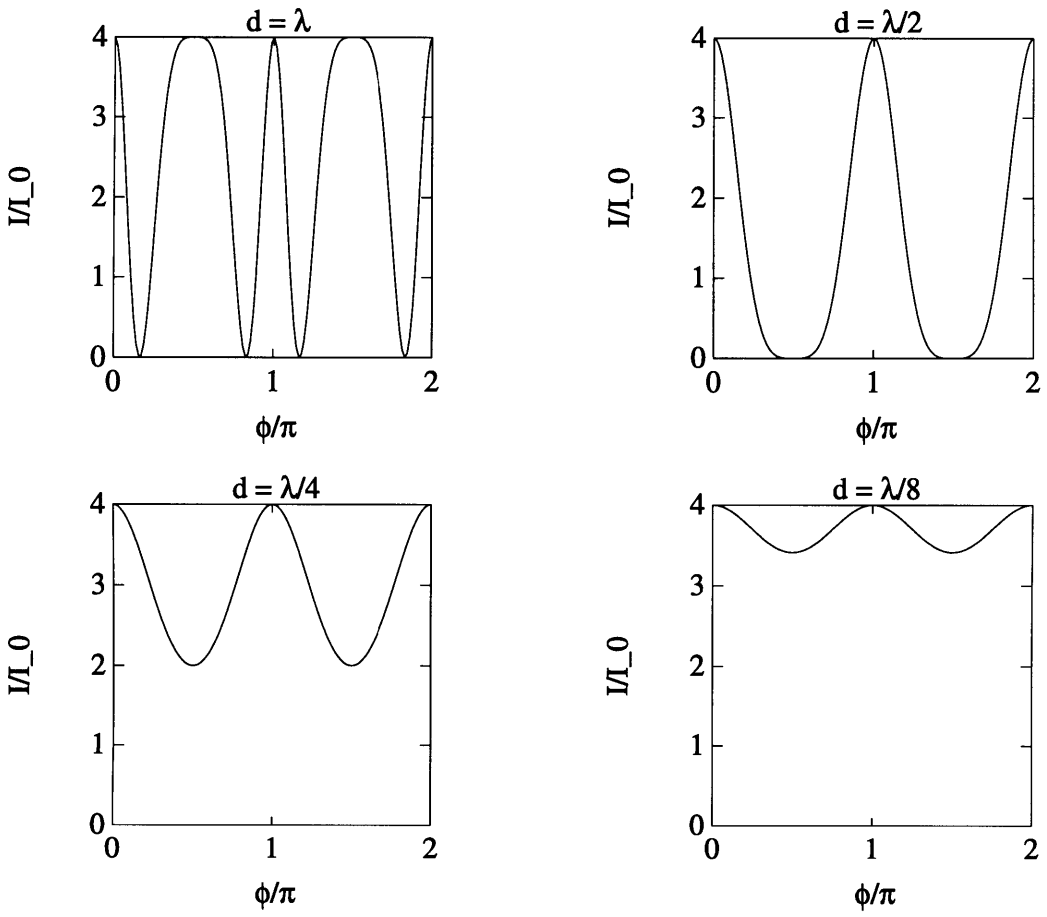

Figure 3-3: Interference Patterns for Two CW Sources without a Free Surface Plotted as Intensity versus Angle, with zero phase shift

the intensity becomes less directionally dependent. All of the plots have the maximum intensity at $\phi = 0$ as they are always 'in phase' in that direction. For the case in which the separation equals one wavelength, the sound is also in phase in the vertical direction and so there is a maximum intensity downwards and upwards. For a half wavelength separation, the sources are exactly out of phase and there is no response at $\phi = 90^0$. For the case in which the separation is just an eighth of the wavelength, the intensity pattern is very close to the point source case.

3.3 Multiple Source Interference

3.3.1 Analysis Using Complex Numbers

Complex numbers can simplify the analysis of the interference of multiple sources (see Clay and Medwin, 1976). Many operations involve the sums and differences of angles and the products of trigonometric functions. These operations are simplified by using the relations between trigonometric functions and complex exponential functions.

$$e^{i\Phi} = \cos\Phi + i\sin\Phi \tag{3.11}$$

$$\cos\Phi = \frac{e^{i\Phi} + e^{-i\Phi}}{2}, \sin\Phi = \frac{e^{i\Phi} - e^{-i\Phi}}{2i} \tag{3.12}$$

For N sources evenly spaced over a distance W, the separation of neighboring sources is:

$$d = \frac{W}{N-1} \tag{3.13}$$

and the pressure fluctuation, $\Delta\rho_n$, of the signal from the nth source, relative to the source at the distance R, is

$$\Delta\rho_n = aexp[i(\omega t - kR + \frac{nkW\sin\phi}{N-1})] \tag{3.14}$$

where a is a constant.

So, the pressure fluctuation of n sources is

$$\Delta\rho = aexp[i(\omega t - kR)] \sum_{n=0}^{N-1} exp(\frac{inkW\sin\phi}{N-1}) \tag{3.15}$$

Since $\omega t - kR$ is common to all the signals, we factor it at the beginning and then suppress it by calculating C as follows:

$$C = a\sum_{n=0}^{N-1} exp(\frac{inkW\sin\phi}{N-1})$$

$$= a\sum_{n=0}^{N-1} exp(inkd\sin\phi)$$

We can show that (see p. 46, Clay and Medwin, 1976):

$$C = Na\{\frac{exp[iNk(W/2)\frac{\sin\phi}{N-1}]}{exp[ik(W/2)\frac{\sin\phi}{N-1}]}\}\frac{\sin[Nk(W/2)\frac{\sin\phi}{N-1}]}{N\sin[k(W/2)\frac{\sin\phi}{N-1}]} \tag{3.16}$$

The expression in braces has an absolute value of 1 and specifies a phase shift that depends on the choice of origin. The remaining factor is known as the "directional response", D, which is:

$$D = \frac{\sin(\frac{N}{N-1}\frac{kW}{2}\sin\phi)}{N\sin(\frac{1}{N-1}\frac{kW}{2}\sin\phi)} \tag{3.17}$$

When N is large, and using

$$\sin[k(W/2)(\sin\phi/(N-1))] \approx k(W/2)(\sin\phi)/(N-1) \tag{3.18}$$

D becomes

$$D = \frac{\sin\frac{kW\sin\phi}{2}}{\frac{kW\sin\phi}{2}} \tag{3.19}$$

The latter expression has the form $(\sin x)/x$ which has a maximum of one as x tends to zero. This is identical to the directional response of a continuously distributed line source (Clay and Medwin, 1976).

If we substitute $\delta = kd\sin\phi$ (d is the distance between two neighboring sources) into C, we have

$$C = Naexp[ik(W/2)\sin\phi]\frac{\sin[Nk(d/2)\sin\phi]}{N\sin(k(d/2)\sin\phi)}$$

$$= aexp[i(N-1)\frac{\delta}{2}]\frac{\sin\frac{N\delta}{2}}{\sin(\delta/2)}$$

So, we have the expression for the energy intensity of n equally spaced sources (denoting $I_0 = a^2$)

$$I = I_0 * (\frac{\sin\frac{N\delta}{2}}{\sin\frac{\delta}{2}})^2 \tag{3.20}$$

Figures 3-4 and 3-5 show us the situation without considering a free surface. The plots have the following characteristics:

- When the sources are in phase (as $d\sin\phi = \pm k\lambda$), the intensity reaches its maximum ($I = N^2 I_0$). As for the two source case, when the sources are in-phase, there is always a maximum response horizontal to the vertical array which is independent of the distance between the sources. More importantly, the maximum direction stays the same when we add more sources to the array because the new sources are still in phase with the old sources.

- Also, we notice that in the direction of maximum intensity, all of the sources must be in phase with each other.

- Generally, nodes in the beam pattern increase as the number of sources increases. In theory, at the position that $\delta = \pm\frac{2k'\pi}{N}$, $k' = 1, 2, \ldots, (N-1), (N+1), \ldots$, (under the condition that $k' \neq 0$) the intensity reaches its minimum $I = 0$.

- Between the minimum position, there are local maximum responses. We can get the local maximum position and its intensity theoretically by letting $\frac{dI}{d\delta} = 0$.

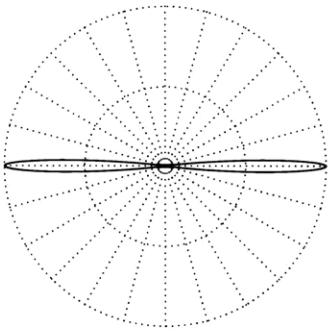

Beam angle = 0 (phase delay = 0)

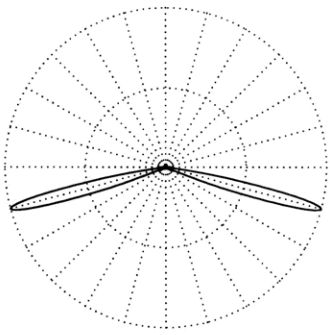

Beam angle = 15 (phase delay = 56.8)

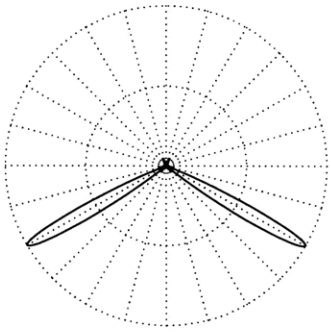

Beam angle = 30 (phase delay = 109.8)

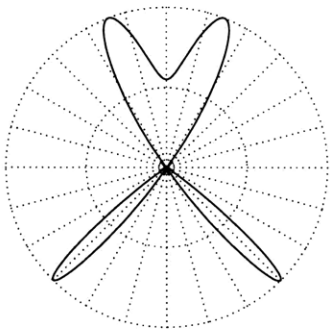

Beam angle = 45 (phase delay = 155.3)

Figure 3-4: Interference Patterns for a Ten Element Array without a Free Surface (I), plotted as rose diagrams

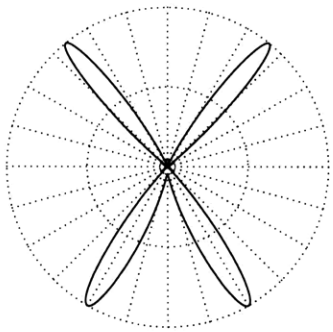

Beam angle = 60 (phase delay = 190.2)

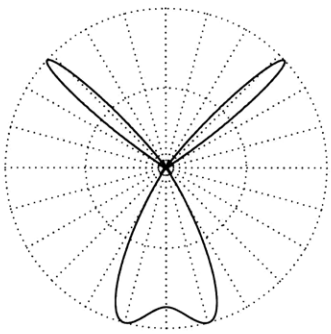

Beam angle = 75 (phase delay = 212.1)

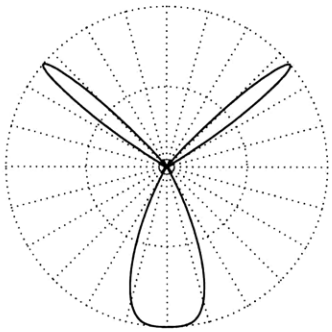

Beam angle = 90 (phase delay = 219.6)

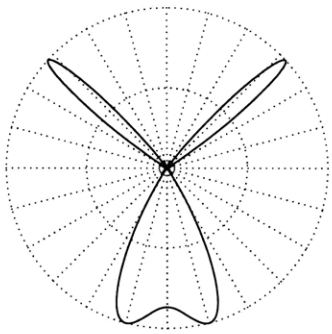

Beam angle = 105 (phase delay = 212.1)

Figure 3-5: Interference Patterns for Ten Sources without a Free Surface (II), plotted as rose diagrams

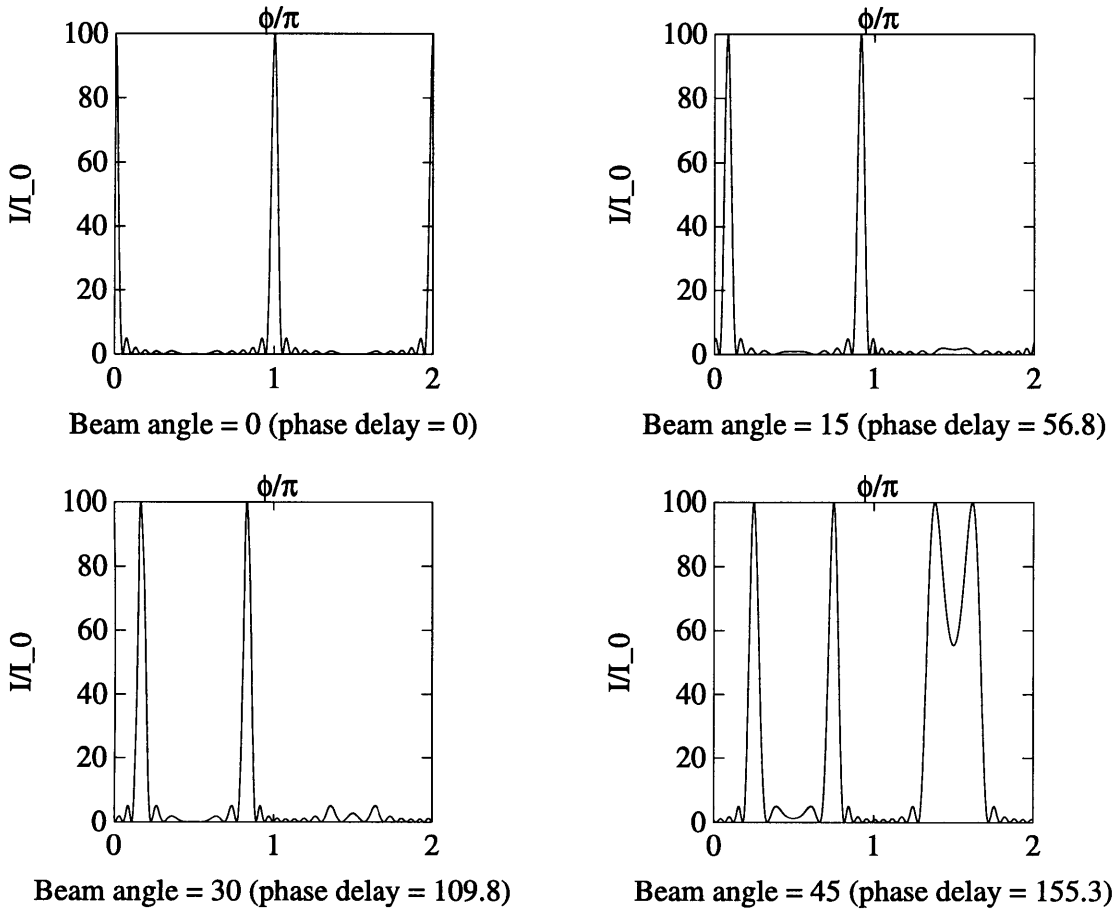

Figure 3-6: Ten Element Array without a Free Surface (I), plotted as intensity versus angle

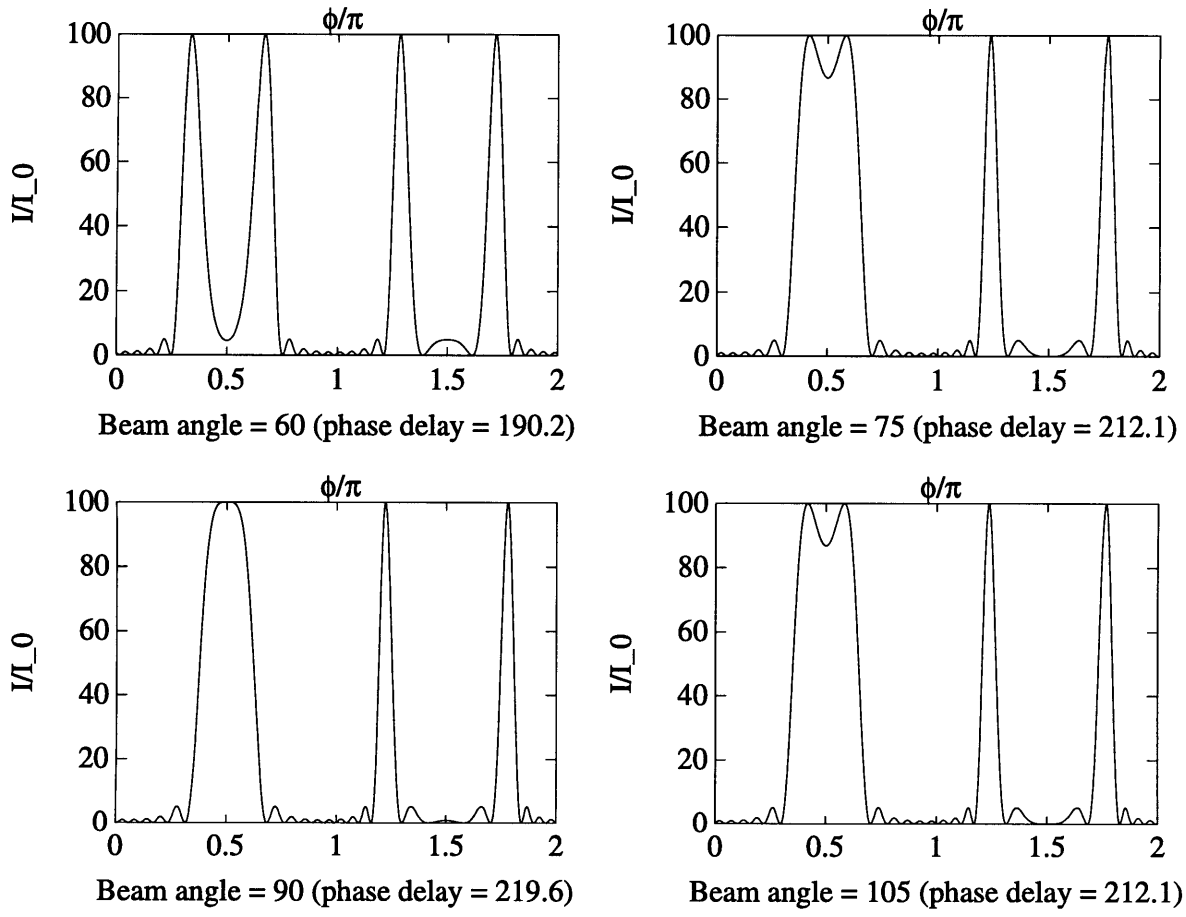

Figure 3-7: Ten Element Array without a Free Surface (II), plotted as intensity versus angle

This leads to positions ($\delta = kd\sin\phi$) at

$$\tan\frac{N\delta}{2} = N\tan\frac{\delta}{2} \tag{3.21}$$

and the local maxima of

$$I = \frac{N^2 I}{1 + (N^2 - 1)\sin^2\frac{\delta}{2}} \tag{3.22}$$

3.3.2 Multiple Sources with a Free Surface

In the case of multiple sources at depth h below a free surface, the fluctuation has two parts, one is directly from the n sources,

$$\Delta\rho_1 = aexp[i(\omega t - kR + kh\sin\phi)]\sum_{n=0}^{N-1} exp(\frac{inkW\sin\phi}{N-1}) \tag{3.23}$$

and the other part corresponds to their images

$$\Delta\rho_2 = aexp[i(\omega t - kR - kh\sin\phi)]\sum_{n=0}^{N-1} exp(\frac{-inkW\sin\phi}{N-1}) \tag{3.24}$$

We have already shown that

$$a\sum_{n=0}^{N-1} exp(\frac{inkW\sin\phi}{N-1}) = aexp[i(N-1)\frac{\delta}{2}]\frac{\sin\frac{N\delta}{2}}{\sin(\delta/2)} \tag{3.25}$$

Similarly we can show that

$$a\sum_{n=0}^{N-1} exp(\frac{-inkW\sin\phi}{N-1}) = aexp[-i(N-1)\frac{\delta}{2}]\frac{\sin\frac{N\delta}{2}}{\sin(\delta/2)} \tag{3.26}$$

So, the total fluctuation is

$$\begin{aligned}\Delta\rho &= \Delta\rho_1 + \Delta\rho_2 \\ &= a\exp[i(\omega t - kR)]\frac{\sin\frac{N\delta}{2}}{\sin(\delta/2)}\end{aligned}$$

$$\left[\exp(i(kh\sin\phi+\frac{(N-1)\delta}{2}))-\exp(-i(kh\sin\phi+\frac{(N-1)\delta}{2}))\right]$$
$$= a\exp\left[i(\omega t-kR)\right]\frac{\sin\frac{N\delta}{2}}{\sin(\delta/2)}*(2i)*\sin(kh\sin\phi+\frac{(N-1)\delta}{2})$$

and the energy density is

$$I_n=4*a^2*(\frac{\sin\frac{N\delta}{2}}{\sin\frac{\delta}{2}})^2*(\sin(kh\sin\phi+\frac{kW\sin\phi}{2}))^2 \tag{3.27}$$

Discussion:

- At the free surface, $\phi=0$ and we can see that for all cases, $I_n=0$.
- If we denote I_{n0} as the energy density for the case of n sources without a free surface, we have

  $$I_{n0}=a^2*(\frac{\sin\frac{N\delta}{2}}{\sin\frac{\delta}{2}})^2$$

  and

  $$I_n=4*I_{n0}*(\sin(kh\sin\phi+\frac{kW\sin\phi}{2}))^2. \tag{3.28}$$

  We can conclude that the free surface effect modifies the energy intensity by a factor of $4*(\sin(kh\sin\phi+\frac{kW\sin\phi}{2}))^2$.

3.3.3 Multiple Sources under a Free Surface with Phase Delay

By modifying the phase difference between two neighboring sources, we can control the outgoing beam direction. Figures 3-4 and 3-5 show the situation without consideration of a free surface. Figures 3-8 and 3-9 show us the interference pattern of 10 sources with different outgoing beam angle with consideration of a free surface.

Assuming that the phase difference between two neighboring sources is the same, with phase advance δ_0, we have

$$\Delta\rho_1=aexp[i(\omega t-kR+kh\sin\phi)]\sum_{n=0}^{N-1}exp(\frac{inkW\sin\phi}{N-1}+\delta_0) \tag{3.29}$$

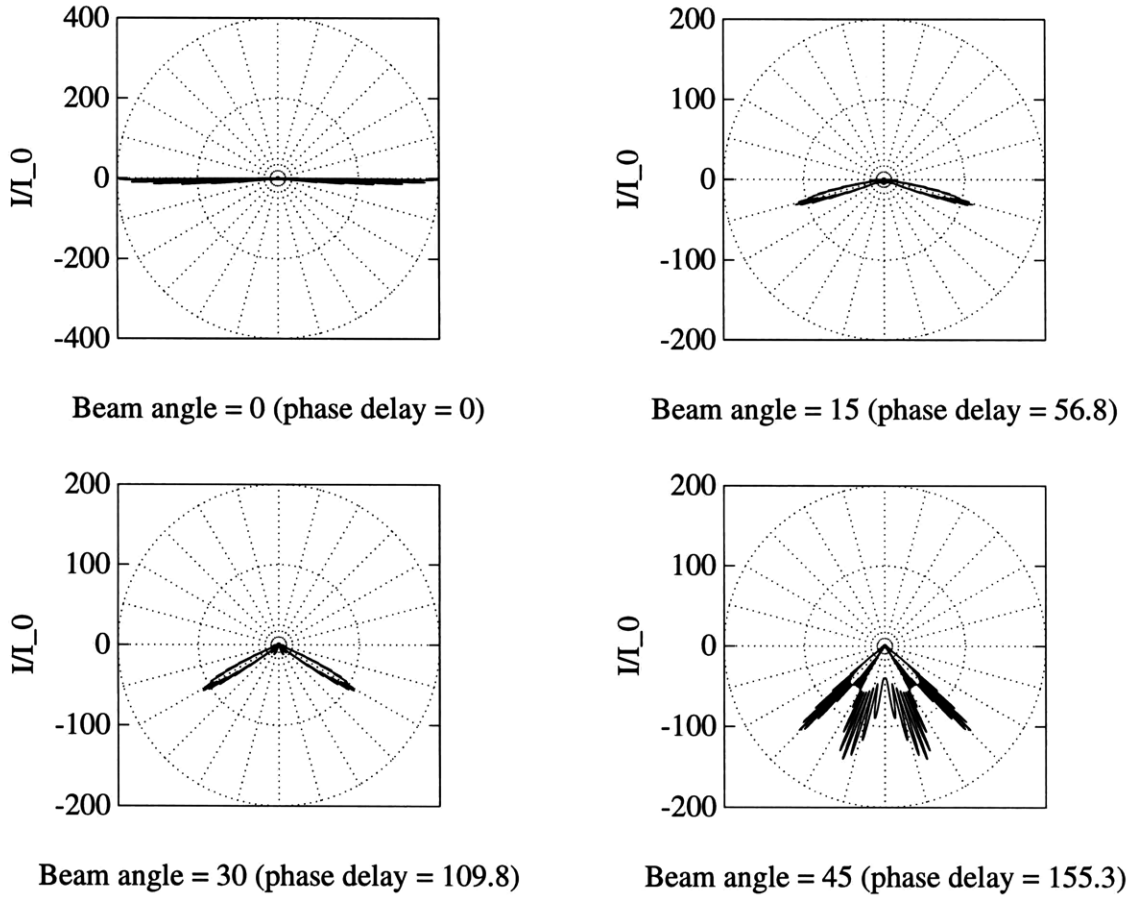

Figure 3-8: Interference Patterns for Ten Element Array with a Free Surface (I), plotted as rose diagrams

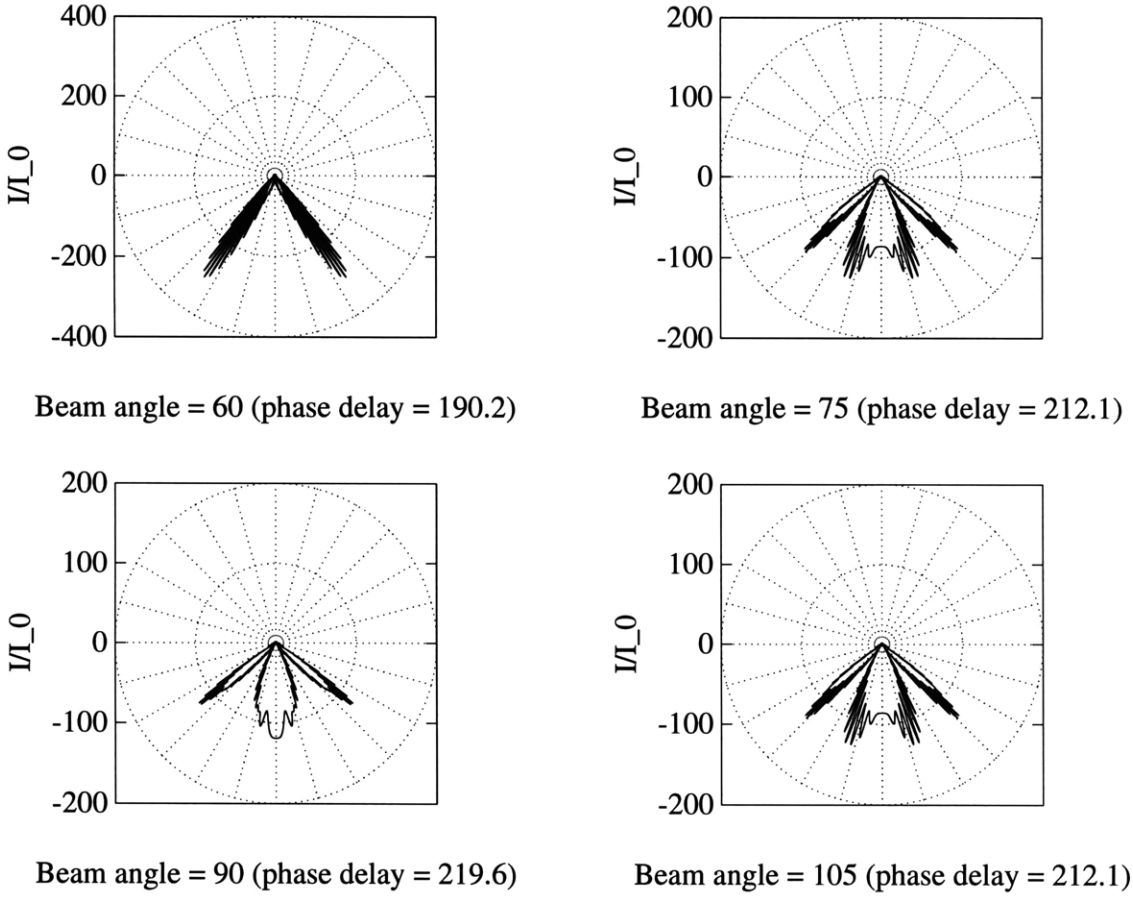

Figure 3-9: Interference Patterns for Ten Element Array with a Free Surface (II), plotted as rose diagrams

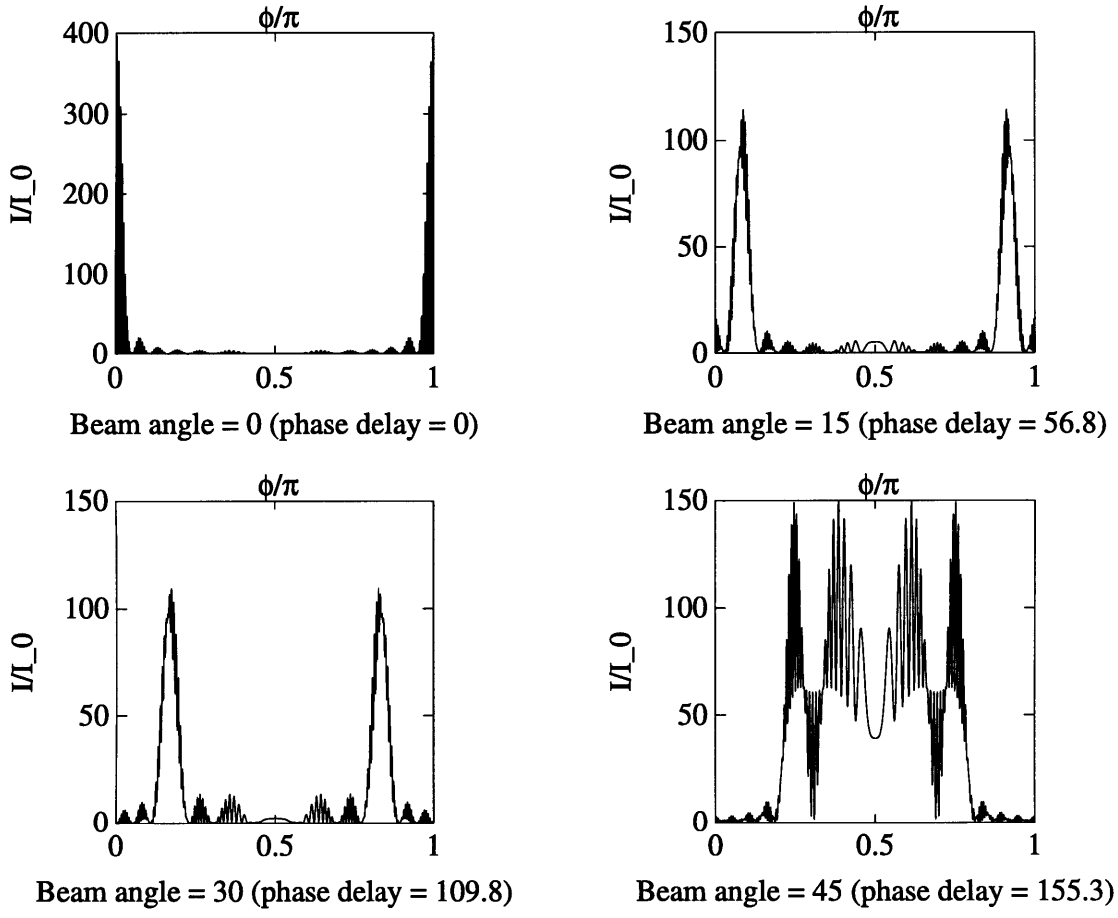

Figure 3-10: Ten Element Array with a Free Surface (I), plotted as intensity versus angle

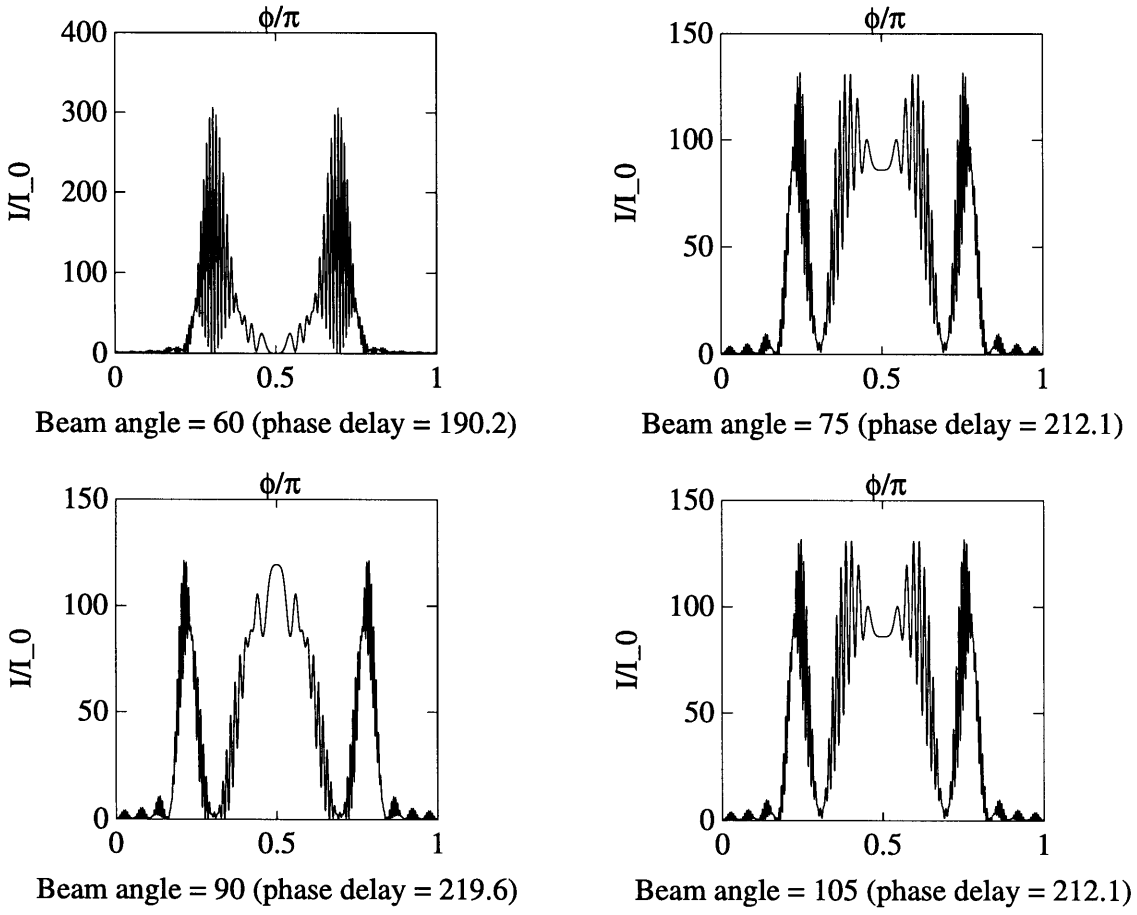

Figure 3-11: Ten Element Array with a Free Surface (II), plotted as intensity versus angle

and another part corresponding to their images

$$\Delta\rho_2 = aexp[i(\omega t - kR - kh\sin\phi)]\sum_{n=0}^{N-1} exp(\frac{-inkW\sin\phi}{N-1} + \delta_0) \tag{3.30}$$

Let $b = \frac{kW\sin\phi}{N-1} + \delta_0$ and $b' = -\frac{kW\sin\phi}{N-1} + \delta_0$, the total fluctuation is expressed as

$$\Delta\rho = aexp[i(\omega t - kR + \frac{N-1}{2}\delta_0)]\{e^{i(kh\sin\phi + \frac{kW\sin\phi}{2})} * \frac{\sin\frac{Nb}{2}}{\sin\frac{b}{2}} - e^{-i(kh\sin\phi + \frac{kW\sin\phi}{2})} * \frac{\sin\frac{Nb'}{2}}{\sin\frac{b'}{2}}\} \tag{3.31}$$

and the energy density is

$$I = A_1 + A_2 - 2 * a^2 * \frac{\sin\frac{Nb}{2}\sin\frac{Nb'}{2}}{\sin\frac{b}{2}\sin\frac{b'}{2}} * \cos(2kh\sin\phi + kW\sin\phi) \tag{3.32}$$

where

$$A_1 = a^2 * \{(\frac{\sin\frac{Nb}{2}}{\sin\frac{b}{2}})^2 \tag{3.33}$$

$$A_2 = a^2 * \{(\frac{\sin\frac{Nb'}{2}}{\sin\frac{b'}{2}})^2 \tag{3.34}$$

When $\delta_0 = 0$, we get the case without phase difference between sources. From equation 3.20, we notice that A_1 is the same as the ten element interference result without a free surface. A_2 is also a ten element interference result, but it has a reversed phase delay corresponding to the image of the vertical array. Also, the part $-2 * a^2 * \frac{\sin\frac{Nb}{2}\sin\frac{Nb'}{2}}{\sin\frac{b}{2}\sin\frac{b'}{2}} * \cos(2kh\sin\phi + kW\sin\phi)$ in the equation 3.32 can be considered as the interference between the ten element array and its image without considering the free surface.

Chapter 4

A Study of a Ten Element Vertical Array in a Depth Dependent Ocean

4.1 Program Development for a Vertical Array

The weakness of the reflectivity model is that it requires large computation time. The original program has noise in the far field, say beyond 30 km offset at 50 Hz. Attenuation is included in order to compress the noise, which alters the result. The new program finds a way to improve the accuracy and also avoids the use of attenuation. In order to improve the accuracy of modeling, we have to make δp very small. While making it smaller, we increase the relative error in the truncation process in the computation, which results in noise in the final modeling(see section 2.3). We get rid of the noise by successfully compressing the truncation error in the far field. The new program is optimized both in speed and structure of the program. Also, a new plotting program was written in matlab 4.0 to plot the amplitude versus distance.

4.2 New Program Flow Chart

The ocean medium can be assumed to be stratified. The sound speed in the water column is approximated by thin homogeneous layers with small discontinuous jumps in velocity across interfaces. The new program has the following flow chart:

```
Sources Loop
    get the new source depth;
    determine the layer number that the source belong to;
    change the model so that the source is on the top the layer;

    get the receivers depths;
    determine the layer number that the receivers belong to;
    change the layer so that the receivers are on the top the layer;

  Frequency Loop
    Layer Loop
      p loop
        Iteration equations to compute the downward(also upward)
           looking reflection and transmission coefficient matrices.
      end{p loop}
      If source layer then {write down its reflection
         and transmission coefficient matrices. }
      If receiver layer then {write down its reflection
         and transmission coefficient matrices. }
    end{Layer Loop}

    Receiver Loop
      x loop
        p loop
          integrate over p to transform p to x
```

```
        end{p loop}
      end {x loop}
    end{Receiver Loop}
       multiply the phase delay factor to the source response
  end{Frequency Loop}
   sum the new source response to total update sources response
end{Sources Loop}
```

It is easy to get the vertical array response. We simply edit a file which has sources and receiver information. Generally, it works as follows:

- Get the new source depth, which is always deeper than the previous one. The distance between sources stays the same and so the new source is always the same distance deeper than the previous one.
- Determine the layer numbers for the new sources and receivers. The program requires that the sources and receivers should be on the top of a layer. It changes the thickness of neighboring layers so that adding sources will not affect the other parts of the layer model.
- Get the source response.
- Multiply the response by the phase delay factor to get the response relative to the top source.
- Sum up all of the responses to get the multiple source response.

4.3 Reflectivity Modeling

4.3.1 Speed of Sound and Ray Paths in the Ocean

The sound travel path is associated with the dependence of the sound speed on depth. Simplifying the results of the Naval Research Laboratory studies (Medwin, 1975), the

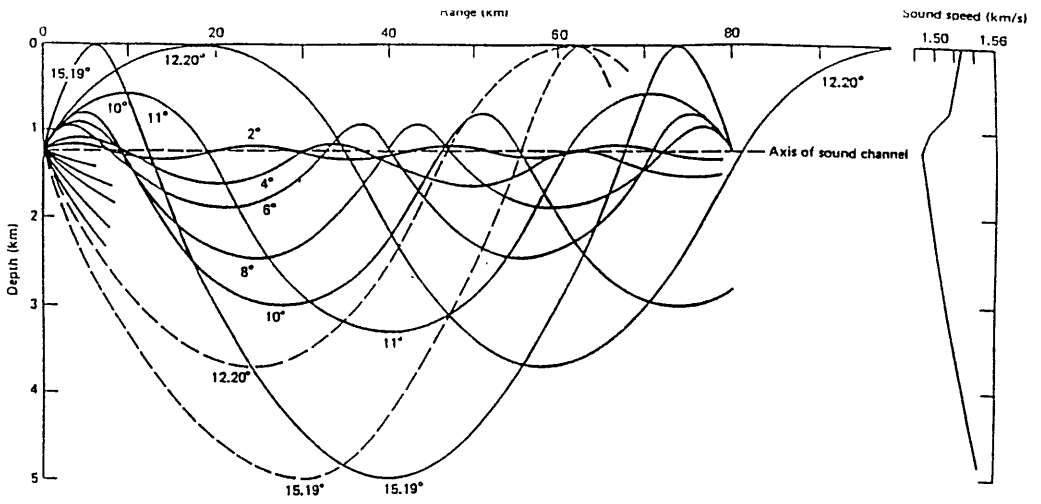

Figure 4-1: Ray diagram for typical Atlantic Ocean sound channel, depicting channeled rays and refracted-surface-reflected(RSR) rays; sound speed profile is at the right. The angles are grazing angles at the axis of the sound channel. (Ewing and Worzel, 1948.)

dependence of sound speed on temperature, salinity, and pressure within 1 km of the surface is found to be approximately

$$c = 1449.2 + 4.6T - 0.055T^2 + 0.00029T^3 + (1.34 - 0.010T)(S - 35) + 1.58 \times 10^{-6} P_a \quad (4.1)$$

where c = sound speed (m/s), T = temperature (^0C), S = salinity (ppt), P_a = gauge pressure due to water column, (N/m^2).

Ignoring compressibility $P_a = \rho_a g z$ and using $\rho_A \approx (1 + S \times 10^{-3})$ kg/m^3, $g = 9.8 m/s^2$, and z = depth(m), the pressure term can be obtained.

When the temperature has a large decrease with increasing depth, the temperature effect overrides the pressure effect and the sound speed gradient is negative, otherwise, the sound gradient is positive.

This vertical stratification of the deep ocean and the resulting ray paths depends on location, season, and time of day. The Figure 4-1 shows the ray traces computed by Ewing and Worzel (1948) as well as the sound profile. The steepest ray shown just grazes the bottom. The angles are measured relative to the horizontal in long-range ray tracing and are called "grazing angles".

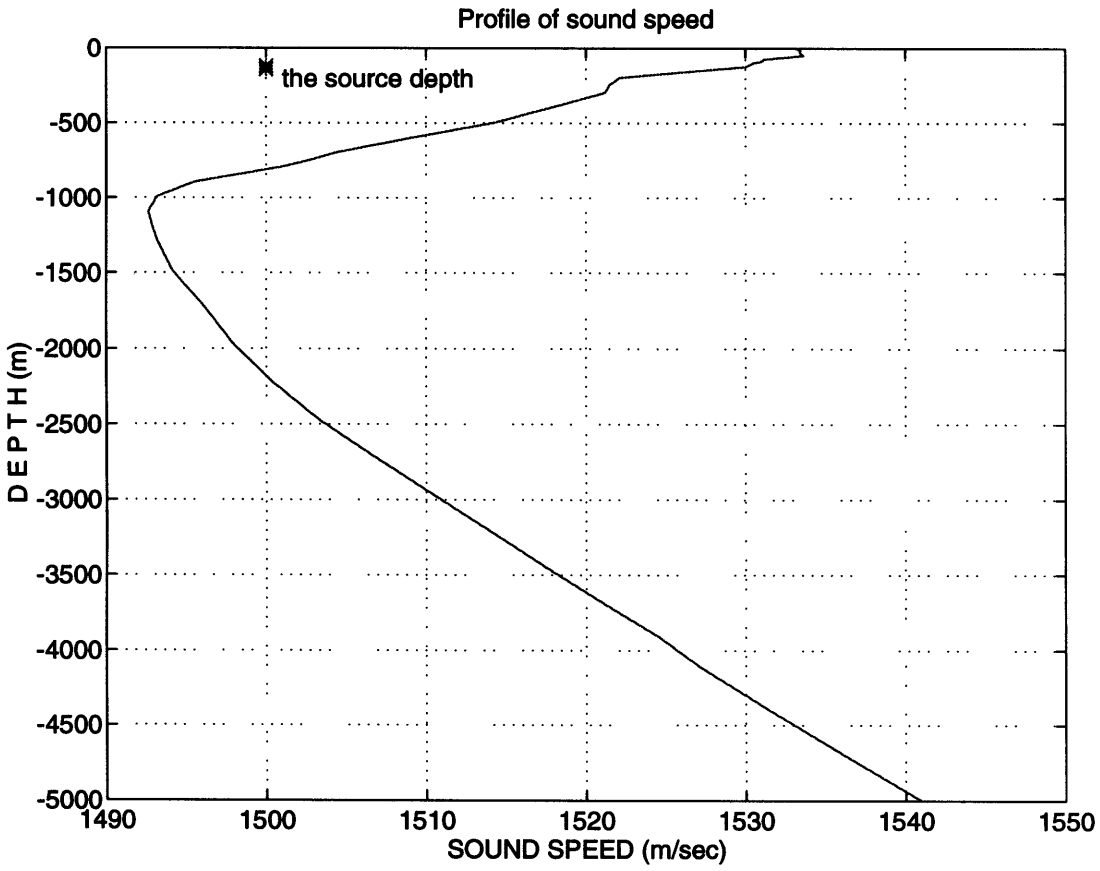

Figure 4-2: The profile of sound speed used in the modeling

4.3.2 Model Description

In Figure 4-2, we show the ten element vertical array position and the ocean velocity profile. A total of 172 layers are used to approximate the smooth gradient zones. We put the sources in such a way that all of the sources are in different layers. In this chapter we present results at 50 Hz (compared to 250 Hz in the last chapter). At this frequency the reflectivity solutions are faster and have less noise.

4.3.3 Homogeneous Result

The results for a homogeneous ocean are shown in figures from Figure 4-3 to Figure 4-9. They show that:

- The deeper the receivers are, the closer the modeling result agrees with the theoretical result. We compare the modeling results at 250 meters below the top source of the vertical array with the theoretical results, and find that they are similar in general characteristics but there are differences in the local characteristics. For receivers at 4000 m depth the modeling results agree well with theoretical predictions. The reason for the difference in the receiver responses at 250 m and 4000 m can be deduced from the conditions we put on the theoretical work. We assumed that the receivers were an infinite distance from the vertical array. The receivers at 4000 m depth are much closer to that assumption than those at 250 m. We conclude that the theoretical results hold pretty well in the far field but are less accurate in the near field.

- Comparing the reflectivity results with the theoretical results, we must consider the geometric effect on the responses. The theoretical results assume that all of the receivers are at the same distance from the source, while in our models all of the receivers are laid out horizontally. So, because of the geometric spreading effect, the responses of receivers on the sea floor will be the product of the theoretical results and a geometric spreading factor which is $cos(angle_0)$. The $angle_0$ is the angle between vertical axis and the receiver angle. Because the distance from the source to the receiver is $d = h_0/\cos(angle_0)$, the response

decreases with the distance from the receiver to the source. The response at distance has to be multiplied by the factor of $\cos(angle_0)$ to get the real response on the horizontal receivers.

- For results beyond 30^0 dip angle, the energy focuses mainly between zero offset and 10 km offset. The far offset response is barely noticeable. As the beam becomes directed downwards, there are less variations in the near offset response. The sidelobe has less effect.

- We do not notice much difference in the results between the 60^0, 75^0 and 90^0 beams at $4000m$, except that amplitude decreases as the beam angle increases. The reason that the maximum mainly remains at 1-3 km distance is that in the far field, the response results from sidelobes of the interference pattern.

- The vertical array response can be divided into three components: the vertical array response without free surface, the image of the vertical array response in the homogeneous media, and the interference of the vertical array and its image array. The complex interference between the array and its image introduces the 'finger' feature into the response on the seafloor. The results show that the image of the array response gives a better fit to the vertical array response than the response from the array itself. Also, the theoretical vertical array response shows stronger 'fingering' than the modeling results.

4.3.4 Gradient Ocean Result

The results for the ocean with gradient velocity profile are shown as follows:

- The gradient effect can be seen from Figure 4-11 to Figure 4-16. Unlike the homogeneous situation, the minimum response never goes to zero. This is because the sources are at depths with different velocities and all of the waves reaching the receivers have complex paths. In this case the assumptions for the theory of a homogeneous ocean can not be applied.

- The gradient has the effect of increasing the amplitudes between 25 and 30 km by about 6 dB to the 0^0, 15^0, 30^0 beams. For the rest of the offsets, the modeling results for receivers at a depth of $4000m$ show a good fit to the homogeneous theoretical results. This indicates that for our arrangement of a vertical array, in a general ocean velocity gradient, the beam is affected at some ranges and in our case there is a great increase in amplitude between 20 and 30 km range, especially for 0^0, 15^0 and 30^0 beams. For the rest of the offsets, the beam does not change its characteristics dramatically. We conclude that the gradient in velocity profile has a big impact on the beam pattern.

- We found our results are quite different from the work done by Özlüer using the ray tracing technique, even considering that we used different oceanic velocity models. First, there is no clear indication of the interference between sources and its image on her results which should change the beam pattern dramatically. Second, her results found no indication that the oceanic velocity profile has effects on the beam. Third, our modeling results show interference even beyond 50 km offset. Her results cannot be trusted after 28 km offset. Fourth, our results show patterns due to the complicated interference between sources and their images, her results show a pretty simple interference pattern. Also, our model uses 50 Hz sources and her model used 250 Hz sources which should have much strong interference patterns. It might be helpful if we can redo her work applying our program to the same model. This can be part of future work.

- It would be interesting to investigate the vertical array results of a pulse. Also, studying the wave path using ray tracing techniques might give us more insight into the vertical array response for the gradient ocean. It is believed that several velocity models might need further study.

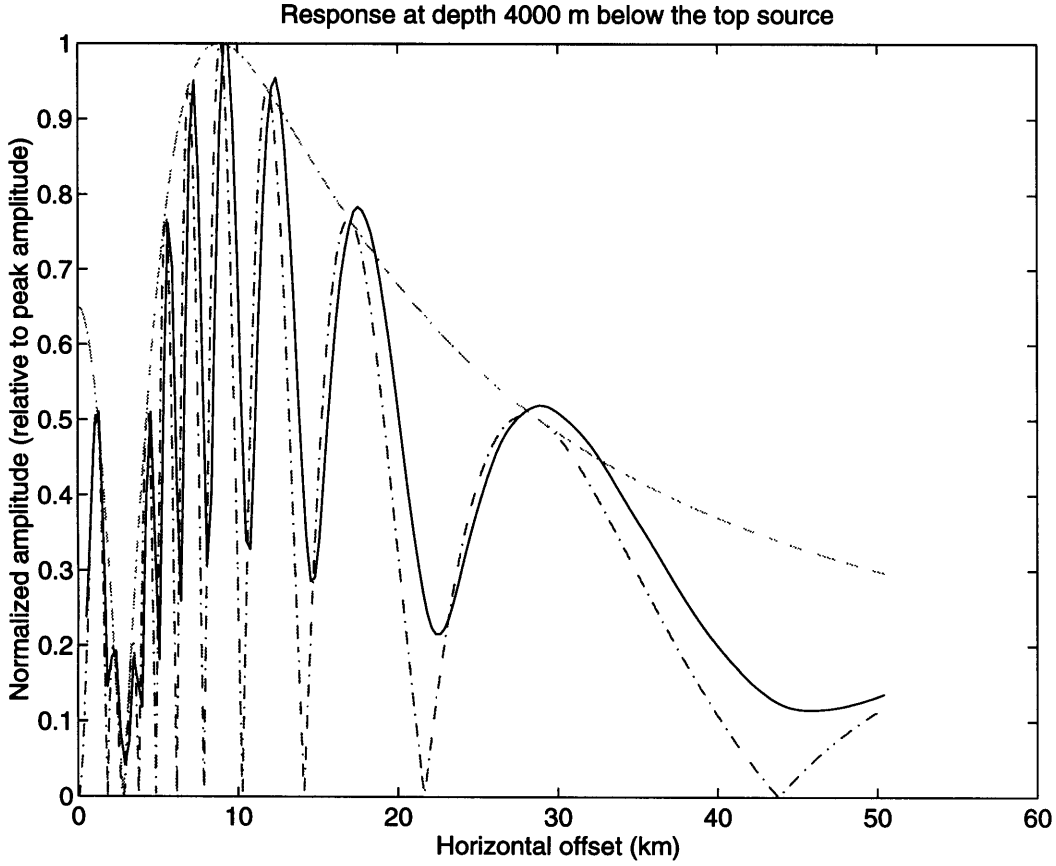

Figure 4-3: The homogeneous ocean response for a 10 element vertical array under a free surface with a 0 degree beam angle. The agreement is good out to 40 km. The solid line is for the reflectivity modeling, the dash-dot line is for theoretical results, the dash line is the theoretical result for the ten element array and also its image (they are the the same). Note that all curves have been normalized to a maximum value of one.

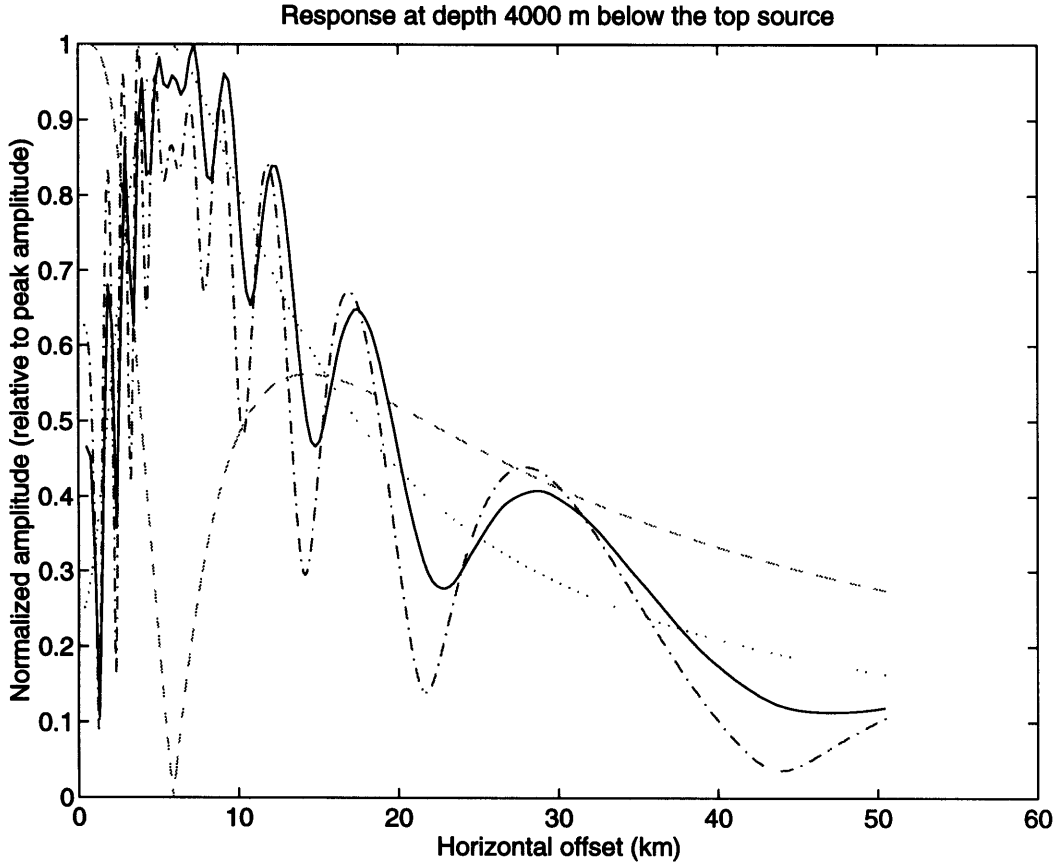

Figure 4-4: The homogeneous ocean response for a 10 element vertical array under a free surface with a 15 degree beam angle. The agreement is good out to 40 km. The solid line is for the reflectivity modeling, the dash-dot line is for theoretical results, the dash line and dots line are the theoretical results for the ten element array and its image respectively. Note that all curves have been normalized to a maximum value of one.

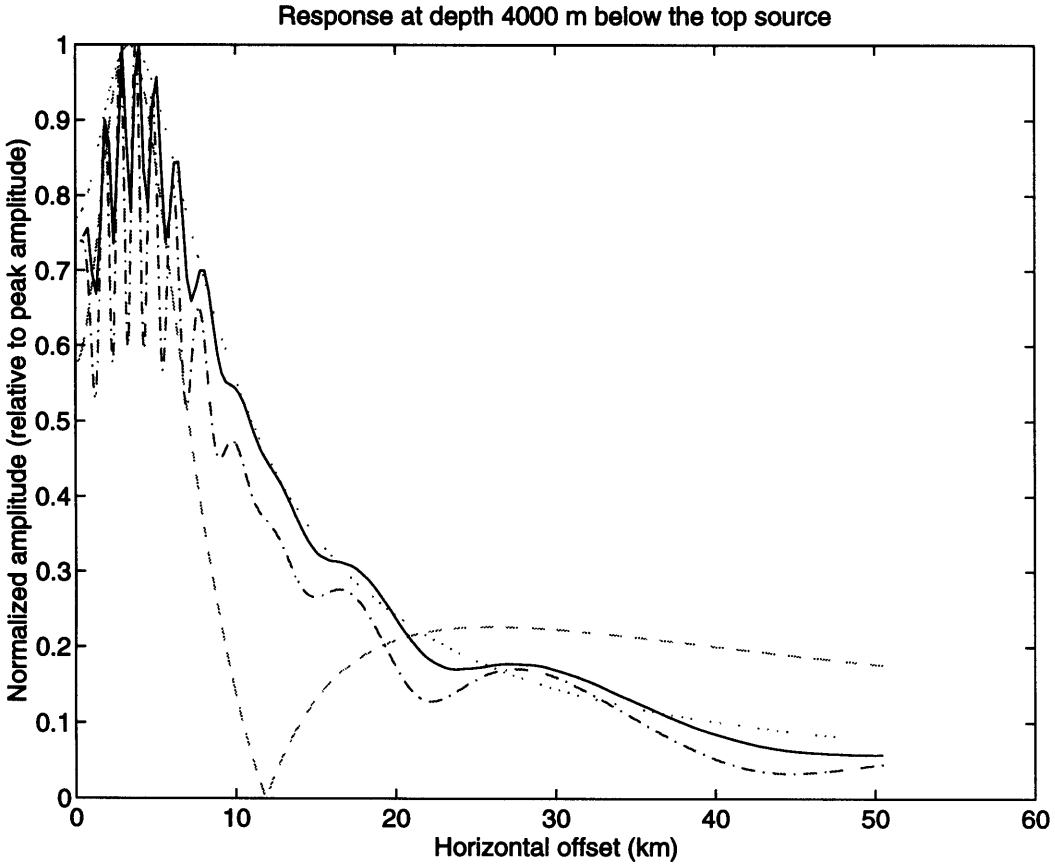

Figure 4-5: The homogeneous ocean response for a 10 element vertical array under a free surface with a 30 degree beam angle. The agreement is good out to 40 km. The solid line is for the reflectivity modeling, the dash-dot line is for theoretical results, the dash line and dots line are the theoretical results for the ten element array and its image respectively. Note that all curves have been normalized to a maximum value of one.

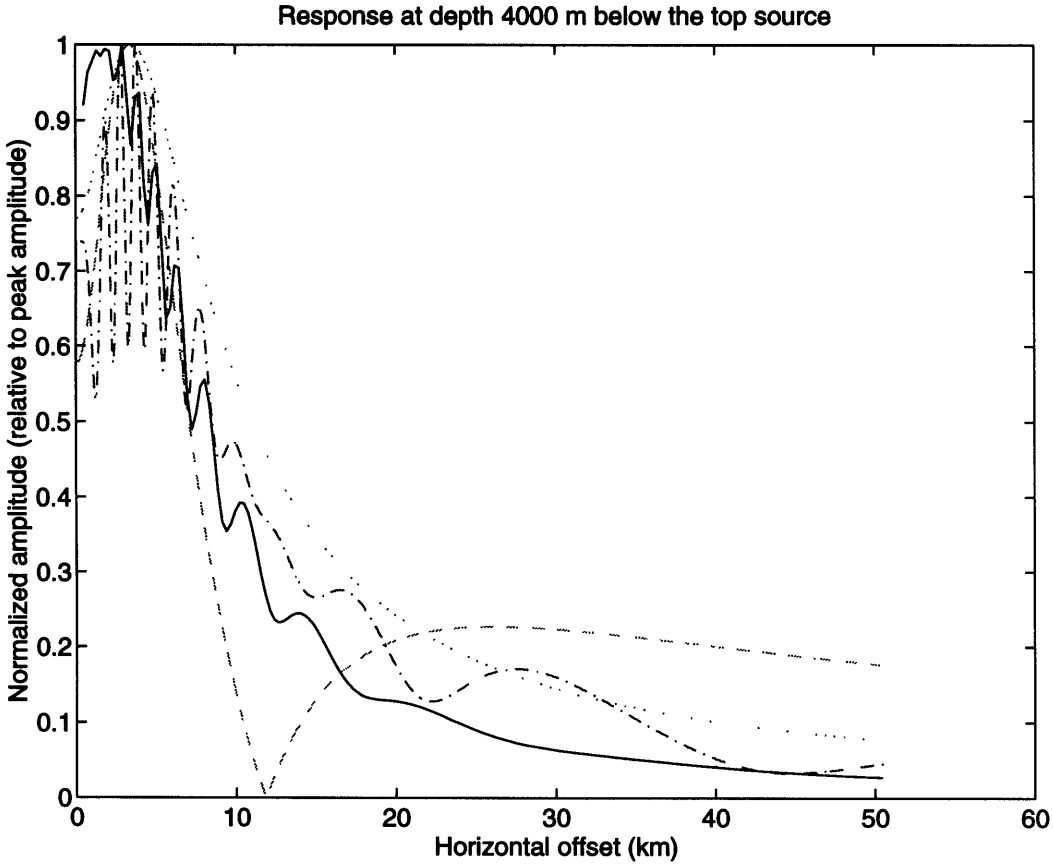

Figure 4-6: The homogeneous ocean response for a 10 element vertical array under a free surface with a 45 degree beam angle. The agreement is good out to 40 km. The solid line is for the reflectivity modeling, the dash-dot line is for theoretical results, the dash line and dots line are the theoretical results for the ten element array and its image respectively. Note that all curves have been normalized to a maximum value of one.

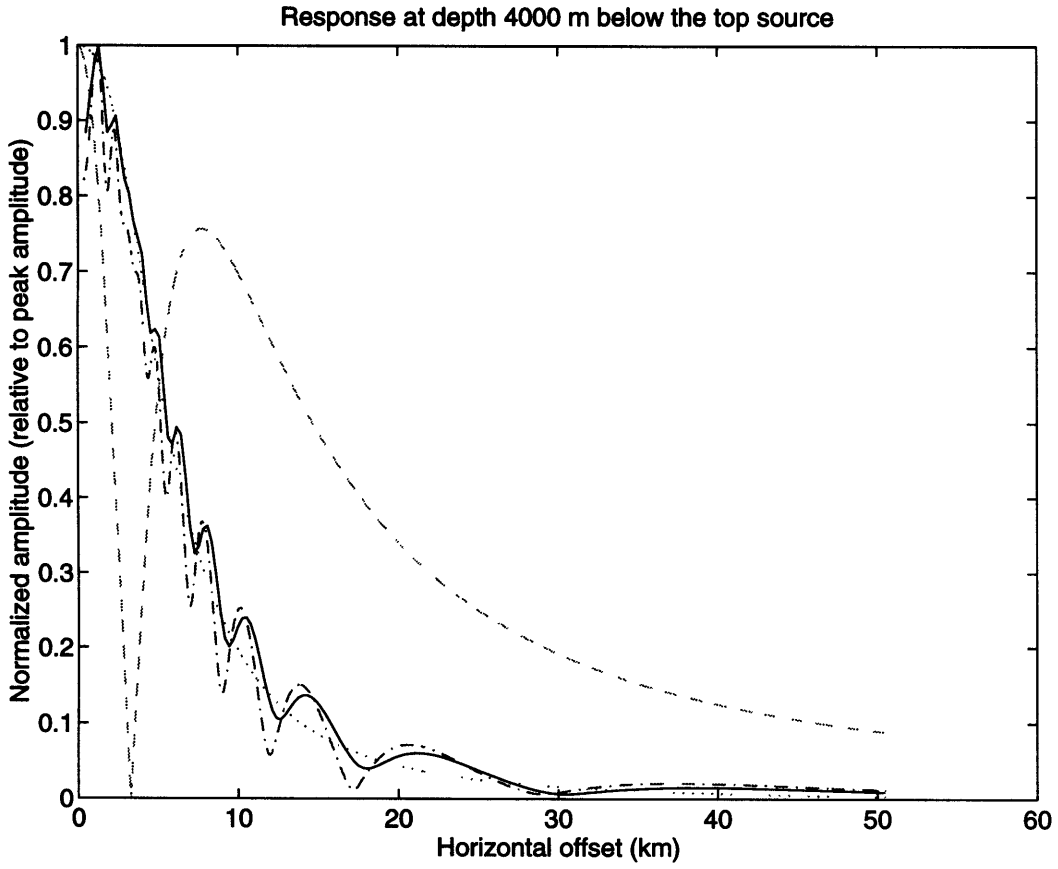

Figure 4-7: The homogeneous ocean response for a 10 element vertical array under a free surface with a 60 degree beam angle. The agreement is good out to 40 km. The solid line is for the reflectivity modeling, the dash-dot line is for theoretical results, the dash line and dots line are the theoretical results for the ten element array and its image respectively. Note that all curves have been normalized to a maximum value of one.

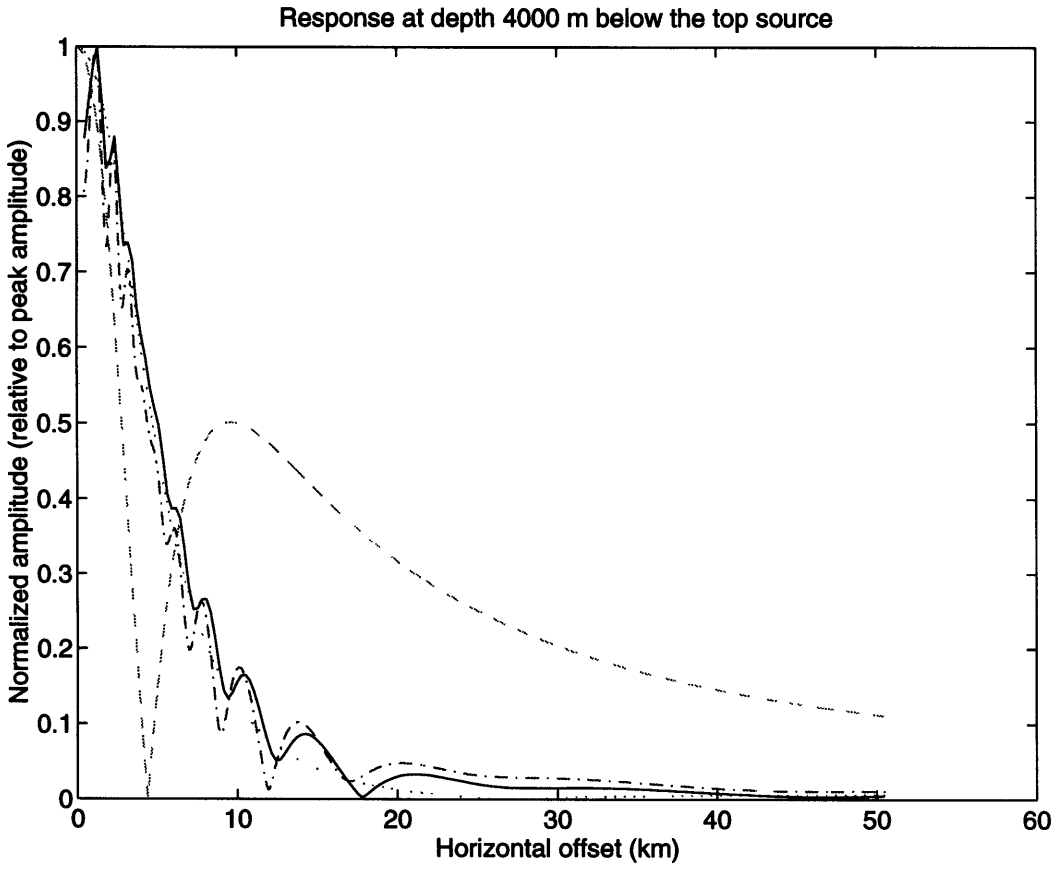

Figure 4-8: The homogeneous ocean response for a 10 element vertical array under a free surface with a 75 degree beam angle. The agreement is good out to 40 km. The solid line is for the reflectivity modeling, the dash-dot line is for theoretical results, the dash line and dots line are the theoretical results for the ten element array and its image respectively. Note that all curves have been normalized to a maximum value of one.

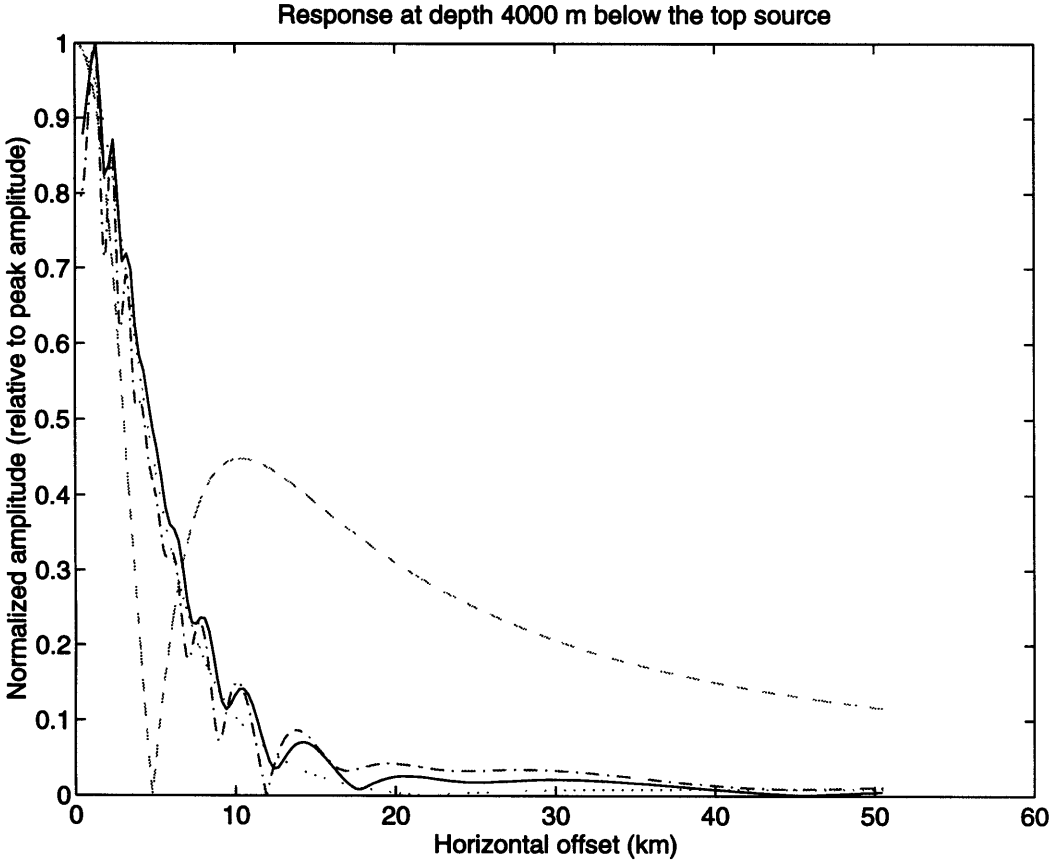

Figure 4-9: The homogeneous ocean response for a 10 element vertical array under a free surface with a 90 degree beam angle. The agreement is good out to 40 km. The solid line is for the reflectivity modeling, the dash-dot line is for theoretical results, the dash line and dots line are the theoretical results for the ten element array and its image respectively. Note that all curves have been normalized to a maximum value of one.

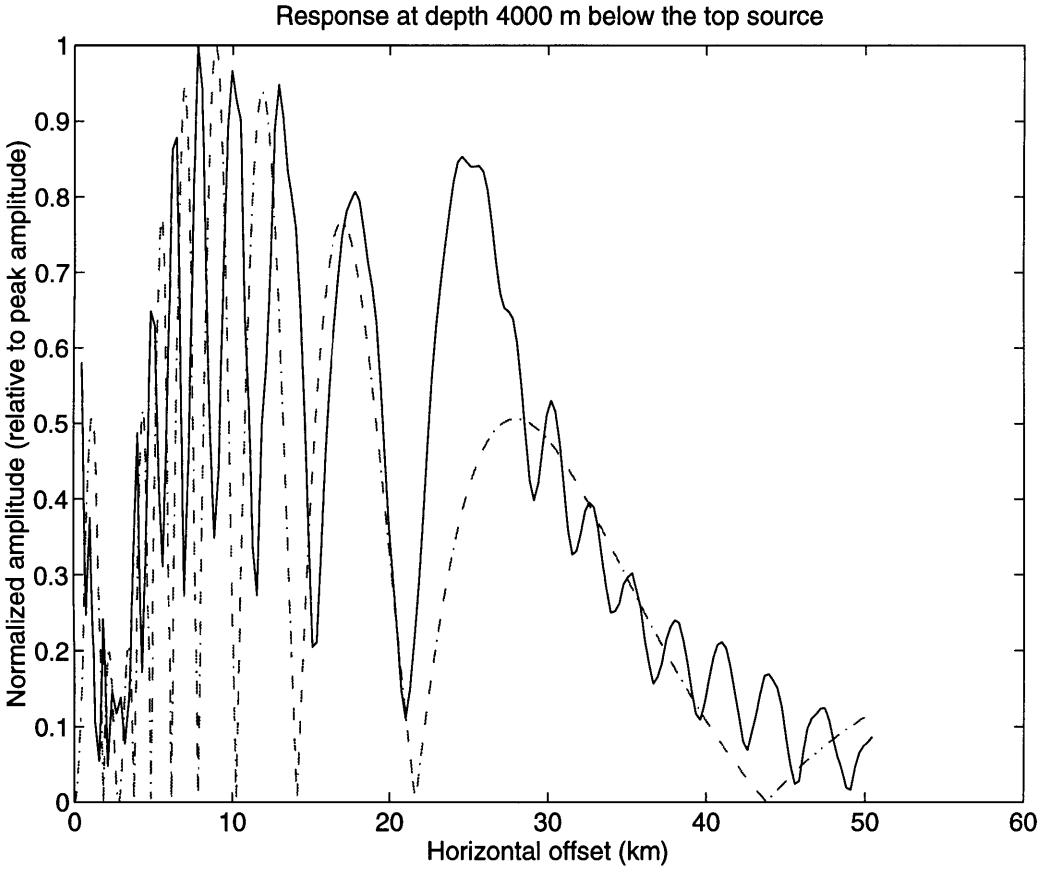

Figure 4-10: The gradient ocean response for a 10 element vertical array (50 Hz) with a 0 degree beam angle (solid line). The gradient has the effect of increasing the amplitudes between 25 and 30 km by about 6 dB. Because of geometrical spreading the largest response at the seafloor occurs at 8 km from side lobes. The dashed line is the theoretical result for the ten element array and is given as a reference. Note that all curves have been normalized to a maximum value of one and it would be useful to compare reflectivity for both homogeneous and gradient models.

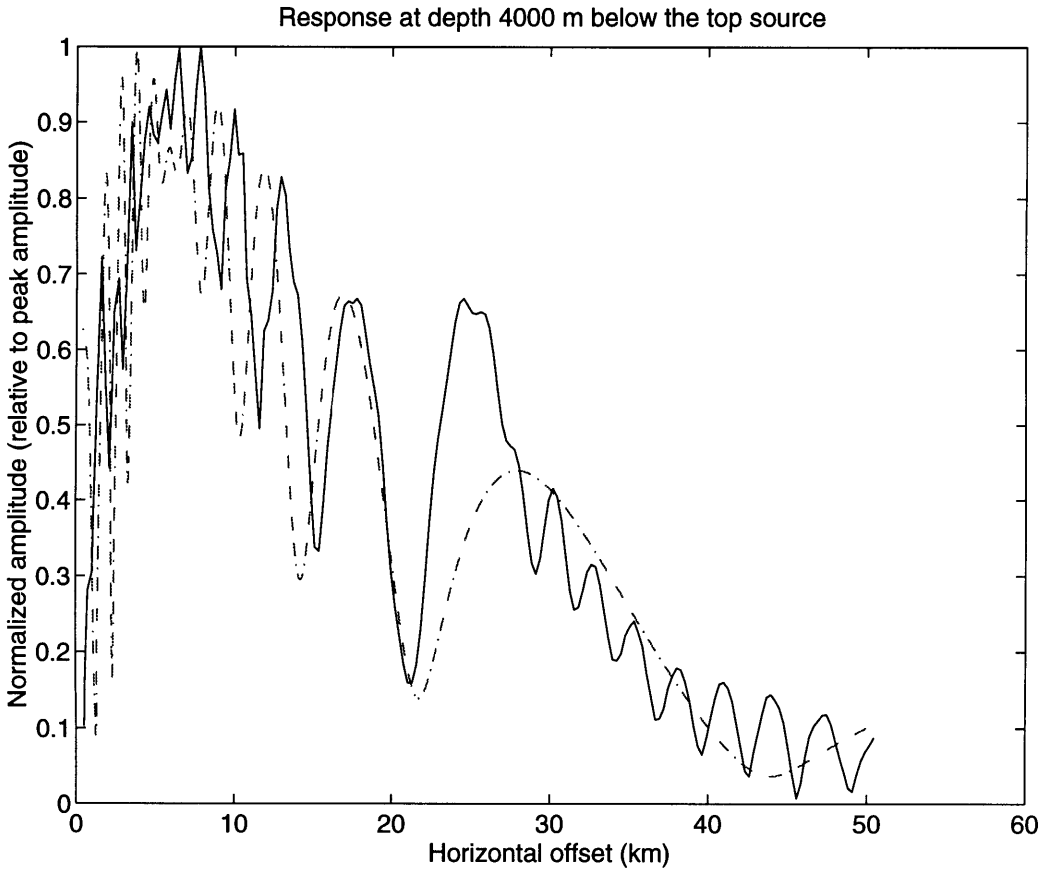

Figure 4-11: The gradient ocean response for a 10 element vertical array (50 Hz) with a 15 degree beam angle (solid line). The gradient has the effect of increasing the amplitudes between 25 and 30 km by about 6 dB. For a homogeneous ocean a 15 degree beam would intersect the seafloor at 15 km. However because of geometrical spreading the largest response at the seafloor occurs at 8 km from side lobes. The dashed line is the same as dash-dot line in the homogeneous ocean response plot and is given as a reference. Note that all curves have been normalized to a maximum value of one and it would be useful to compare reflectivity for both homogeneous and gradient models.

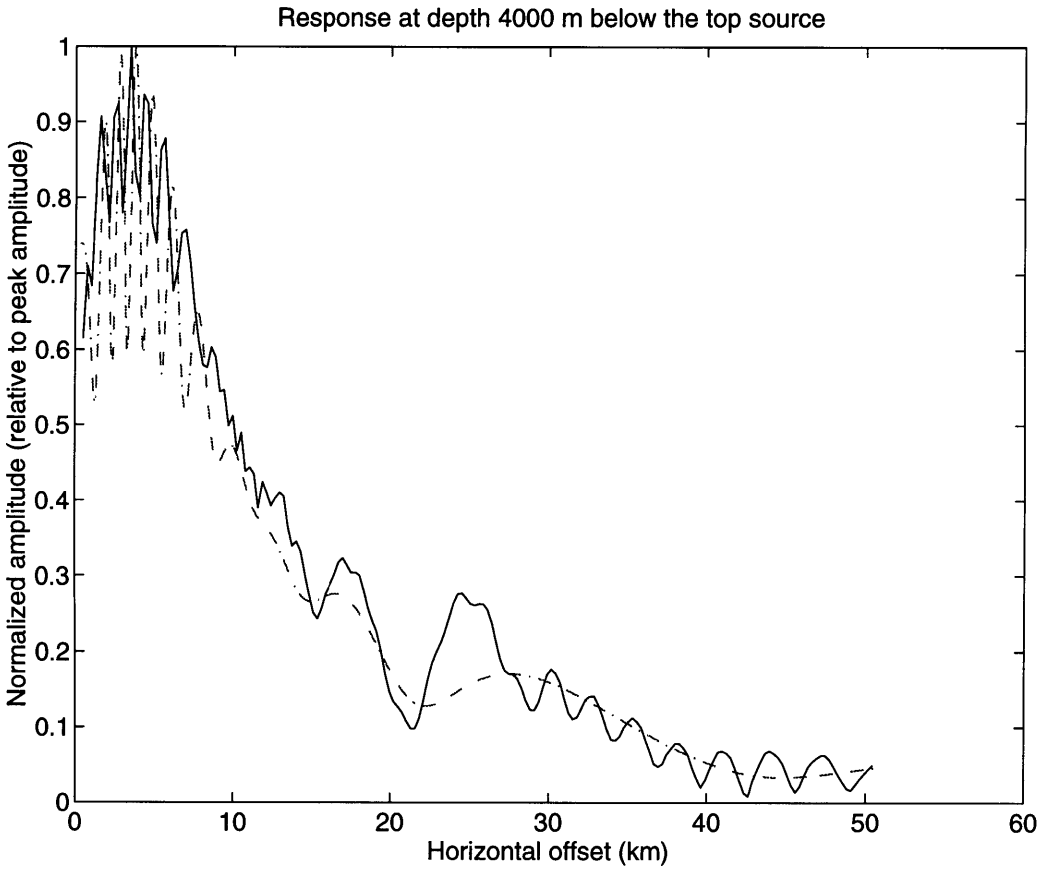

Figure 4-12: The gradient ocean response for a 10 element vertical array (50 Hz) with a 30 degree beam angle (solid line). The gradient has the effect of increasing the amplitudes between 25 and 30 km by about 6 dB. The dashed line is the same as dash-dot line in the homogeneous ocean response plot and is given as a reference. Note that all curves have been normalized to a maximum value of one and it would be useful to compare reflectivity for both homogeneous and gradient models.

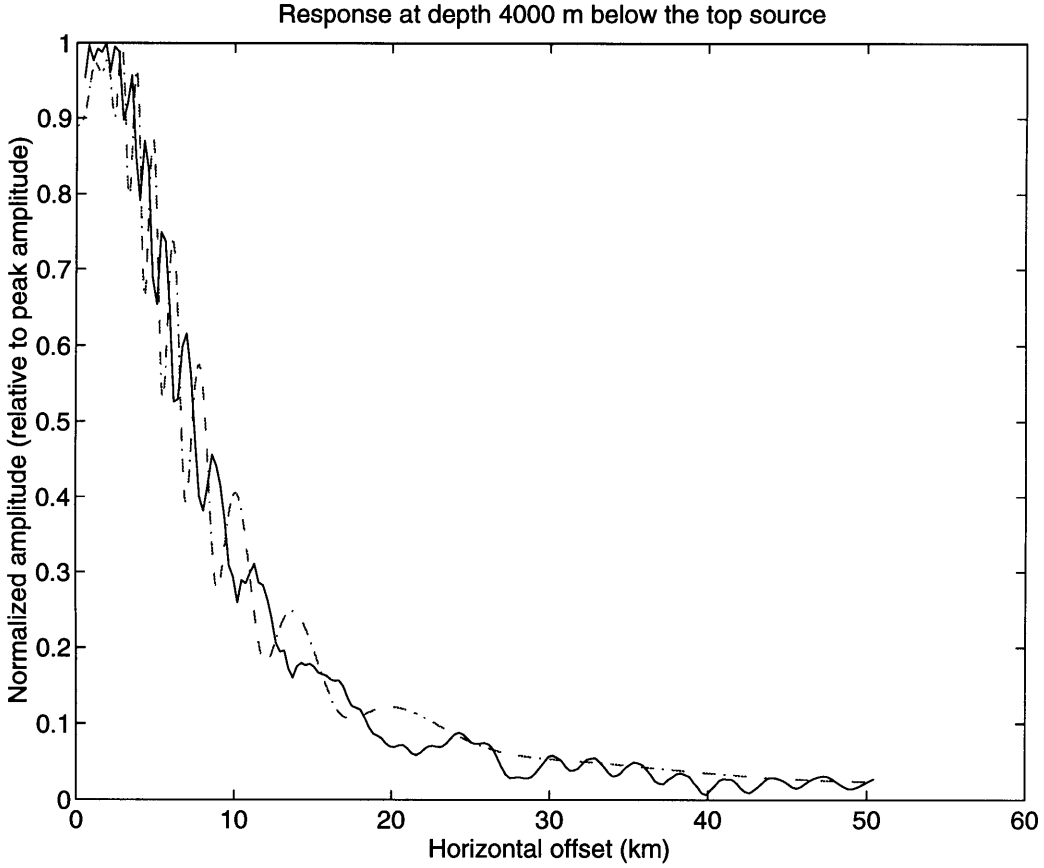

Figure 4-13: The gradient ocean response for a 10 element vertical array (50 Hz) with a 45 degree beam angle (solid line). The gradient has the effect of increasing the amplitudes between 25 and 30 km by about 6 dB. The dashed line is the same as dash-dot line in the homogeneous ocean response plot and is given as a reference. Note that all curves have been normalized to a maximum value of one and it would be useful to compare reflectivity for both homogeneous and gradient models.

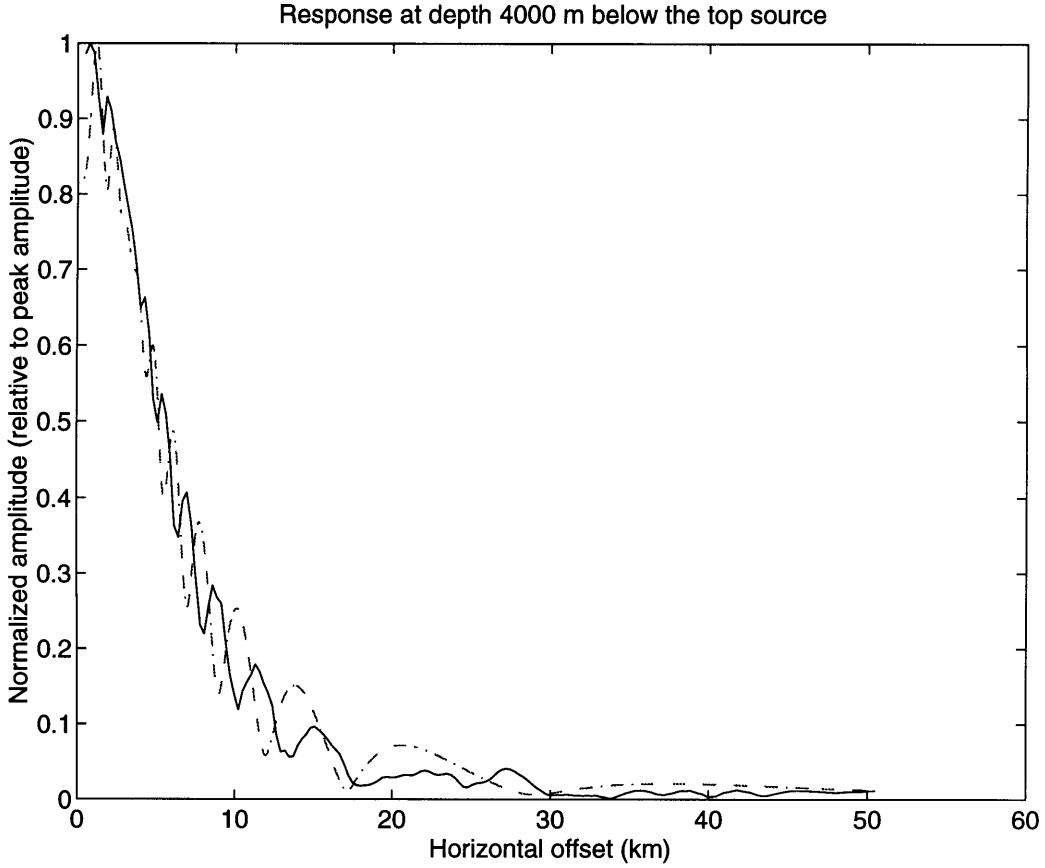

Figure 4-14: The gradient ocean response for a 10 element vertical array (50 Hz) with a 60 degree beam angle (solid line). The gradient has the effect of increasing the amplitudes between 25 and 30 km by about 6 dB. The dashed line is the same as dash-dot line in the homogeneous ocean response plot and is given as a reference. Note that all curves have been normalized to a maximum value of one and it would be useful to compare reflectivity for both homogeneous and gradient models.

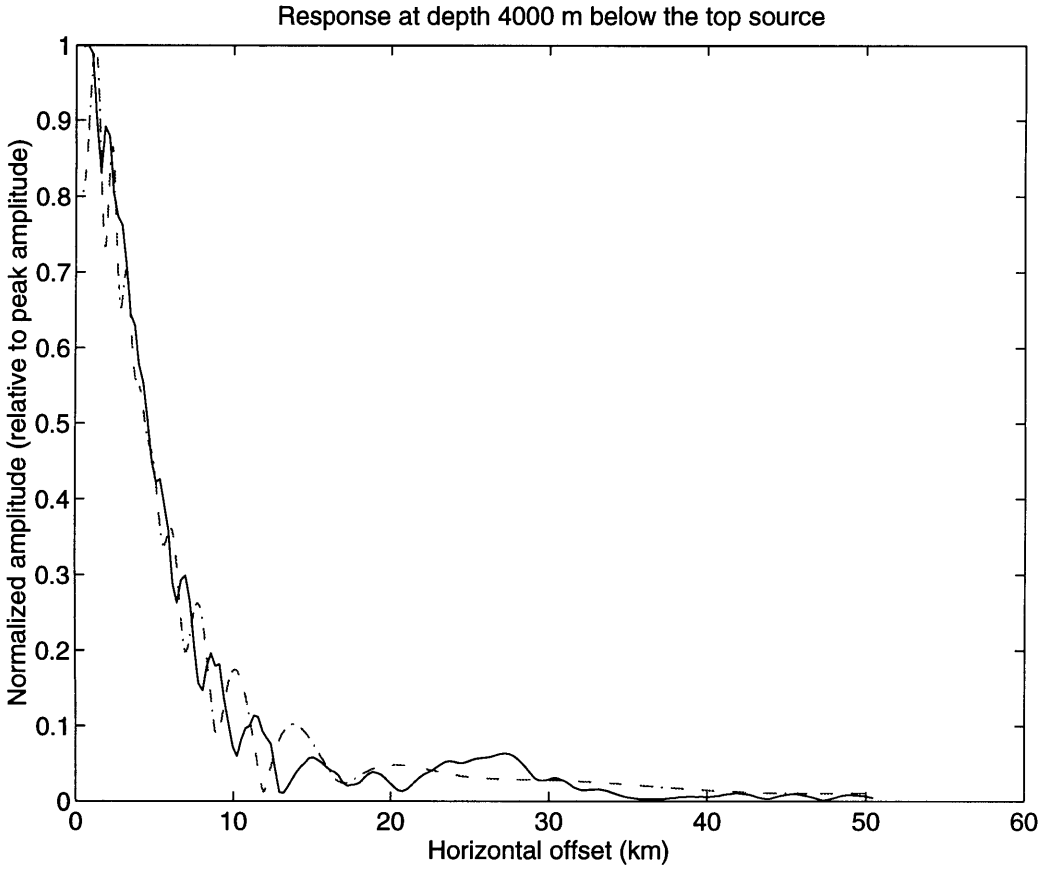

Figure 4-15: The gradient ocean response for a 10 element vertical array (50 Hz) with a 75 degree beam angle (solid line). The gradient has the effect of increasing the amplitudes between 25 and 30 km by about 6 dB. The dashed line is the same as dash-dot line in the homogeneous ocean response plot and is given as a reference. Note that all curves have been normalized to a maximum value of one and it would be useful to compare reflectivity for both homogeneous and gradient models.

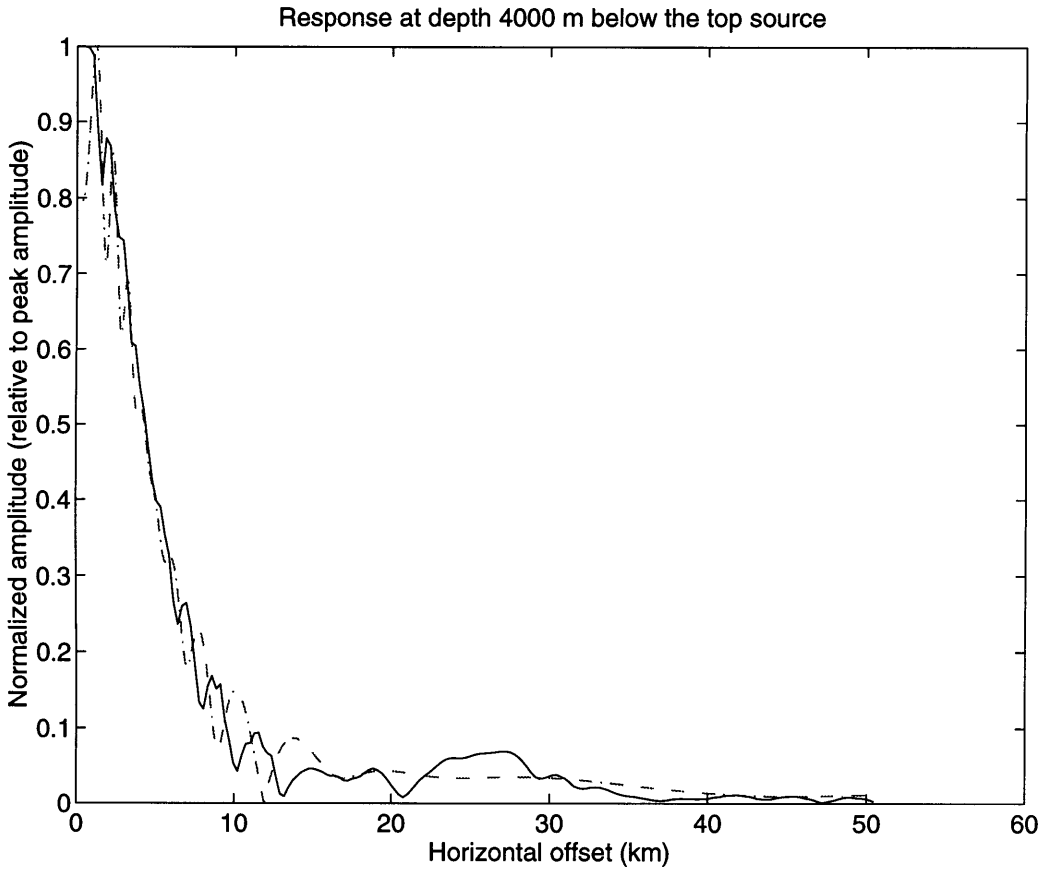

Figure 4-16: The gradient ocean response for a 10 element vertical array (50 Hz) with a 90 degree beam angle (solid line). The gradient has the effect of increasing the amplitudes between 25 and 30 km by about 6 dB. The dashed line is the same as dash-dot line in the homogeneous ocean response plot and is given as a reference. Note that all curves have been normalized to a maximum value of one and it would be useful to compare reflectivity for both homogeneous and gradient models.

Chapter 5

Comparison of Modified Reflectivity Results with Benchmark Solutions

5.1 Test Problem Solutions

In order to test our reflectivity code, we compare solutions of two of seven test problems discussed at the PE Workshop II held in Slidell, LA on 6-10 May 1991 (Jensen, 1993).

5.2 Test Case 1

A point source placed near a reflecting boundary in a homogeneous medium gives rise to the well-known Lloyd-mirror interference pattern for which an exact field solution is available. The Lloyd-mirror pattern is ideal for checking both the angular distribution of energy associated with a given starting field and the high-angle capability of parabolic methods. It is also a simple test for checking the normalization of reflectivity output to transmission loss.

In Test Case 1 the fluid halfspace has a constant speed of 1500 m/s. The source frequency is 40 Hz and the source/receiver depths below the free surface are $350m$ and

$3990m$. The solid line in Fig. 5-1 shows the image reference solution which is known to be exact reference. The reflectivity result is in perfect agreement with the reference solution out to 10 km range at 40 Hz. Numerically stable results were obtained with $\delta p = 0.00005$, starting $p = 0.0$, ending $p = 1.0$. In order to get this agreement a DC offset of 6 dB was applied to the reflectivity result.

5.3 Test Case 7

During PE Workshop II, test case 7 was introduced which reveals serious deficiencies in some PE approximations. The test problem deals with long-range propagation in a surface duct. The source frequency is 80 Hz, which results in a leaky (virtual) mode, which continuously sheds energy into the lower medium, as indicated by the dashed arrows in Figure 7.1 of Jensen, 1993.

The test problem is critical to test that a small phase error for the refracted leaky path can result in large changes in sound level in the duct beyond the first convergence zone. Thus, in the case where the two arrivals (the ducted and the leaky arrival) have similar amplitudes, we may observe level changes of several tens of dB's between constructive and destructive path interference.

The reference solution to this problem for a source at 25 m and a receiver at 100 m was generated by the SNAP normal-mode code. The SNAP reference solution is shown as the solid line in the Fig. 5-2. The reflectivity results are shown as a dashed line. Numerically stable results were obtained with a $\delta p = 0.00005$, starting p = 0.0, ending p = 1.0. The number of layers was 760 which makes a layer thickness of about $\lambda/4$. The results are poorer at coarser thicknesses. When starting receiver range = 0.5 km, ending receiver range = 150.5 km, receiver offset = 0.81 km, The run time on an IBM RS-6000 is 22 minutes and 10 seconds for one frequency (80 Hz).

The results show that the our reflectivity code can handle this problem accurately for 80 Hz to range beyond 100 km. No offset was applied to the reflectivity output to get this agreement.

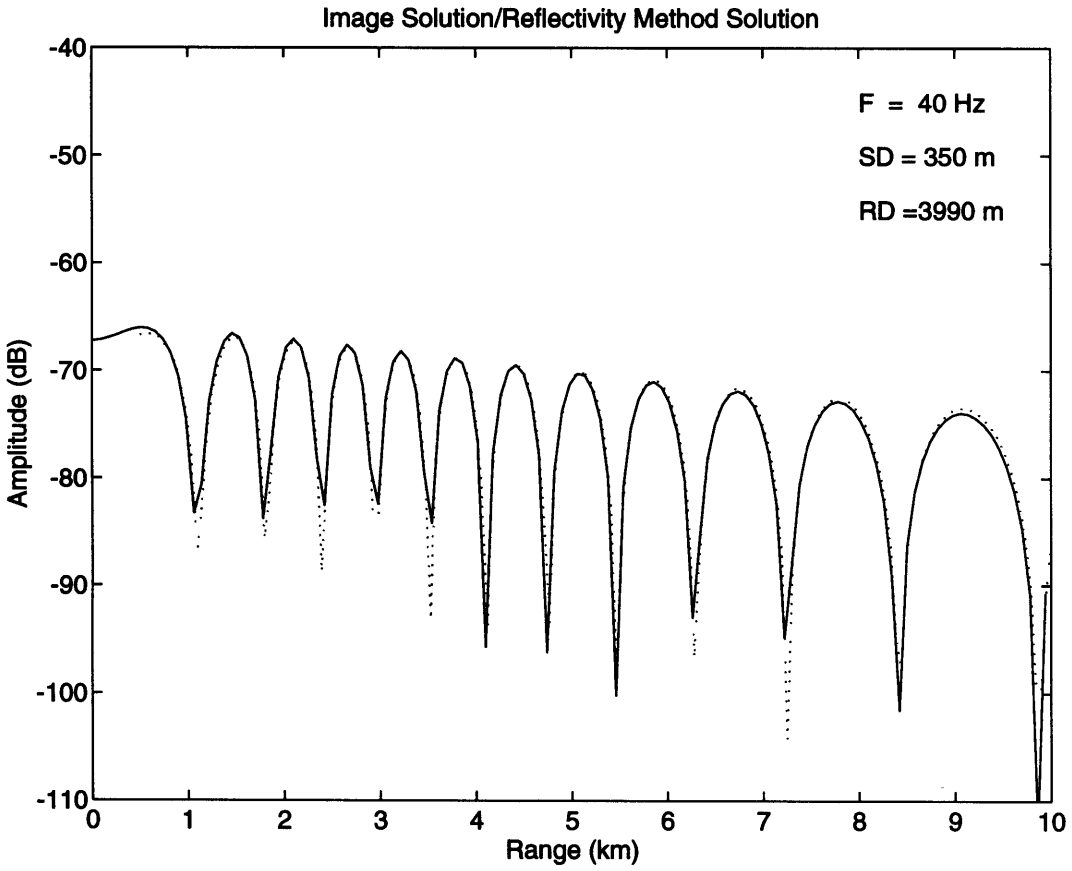

Figure 5-1: Comparison of image reference solution (solid line) with reflectivity result(dotted line)

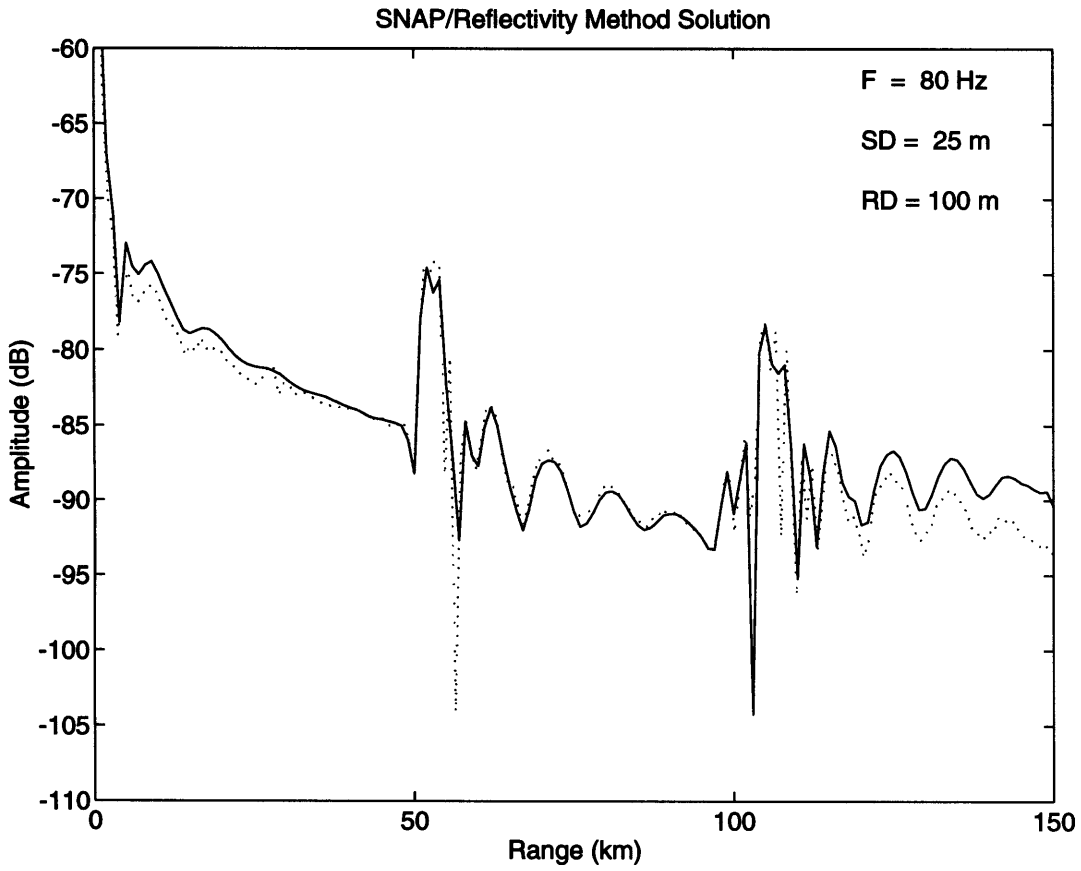

Figure 5-2: Comparison of normal-mode reference solution (SNAP with solid line) with reflectivity result(dotted line)

5.4 Discussion

In order to get correct response in the far field, I modified the original program to get the acurate response in far field. There is the several improvement in the reflectivity code.

- I change the single precision program to double precision which increases the the precision of the program and thus reduces the error of reflectivity result.
- The new program is much simpler which help to reduce unnecessary numerically error. The new program can interpolate the velocity profile in a easy way so that it is easy to decrease the layer thickness until the result convergence. In our practice, we found the reflectivity results converge when the layer thickness is about a quarter of the wavelength.
- It is essential to get the correct result by introducing an attenuation factor in the frequency, which the program uses to get around the singularity pole on the real axis by deforming the integration path. Without attenuation, we cannot get an convergence result for the PE test case 7. The attenuation factor is introduced by making the frequency f_0 complex, which gets new frequency $f = (f_0, decay/(2 * \pi))$, the $decay$ is the attenuation factor. In our calculation, I found we can get quick convergent result by letting $decay = log(1.1)/4$.
- The new program correct attenuation effect on the far field response by multiplying a correction factor, $e^{decay*x}$ where x is the horizontal offset. I found the factor from the equation 2.33, which brings a decay factor after we apply complex frequency by bringing in attenuation.
- The original program does not get amplitude relative to $1m$ from the source which implies that we might use a "magic number". In PE Workshop test 7, we get the results exactly relative to $1m$ from the source. Unfortunately, for the Test case 1, we get to twice big responses applying our modified program. In our future study, we will try to calibrate the source level to get amplitude

relative to $1m$. I believe we might need a factor of frequency difference in the program, because in the PE Workshop test 7 the source frequency is 40 Hz instead of 80 Hz used in PE Workshop test 7.

- Applying the improved program, I get the very far offset response (up to 150 km) of a source in the deep ocean at frequency of 250 Hz, while original program cannot get the response without significant noise beyond 50 km for 50 Hz. Figure 5-3 shows that response of the 250 Hz source on the 250 m and 4000 m receivers below the source using the PE Workshop test 7 model except that it uses 250 Hz source instead of 80 Hz. It is surprising that it do not have any noise as far as 150 km offset. In the result, we notice that the convergence zones are at about 30 km, 75 km, and 140 km offset which confirms Figure 7.1 of Jensen 1993. It needs to mention that the convergence result is gotten when I apply the layer thickness as fine as a quarter of wavelength which is finer than that of 80 Hz in the PE Workshop test 7.

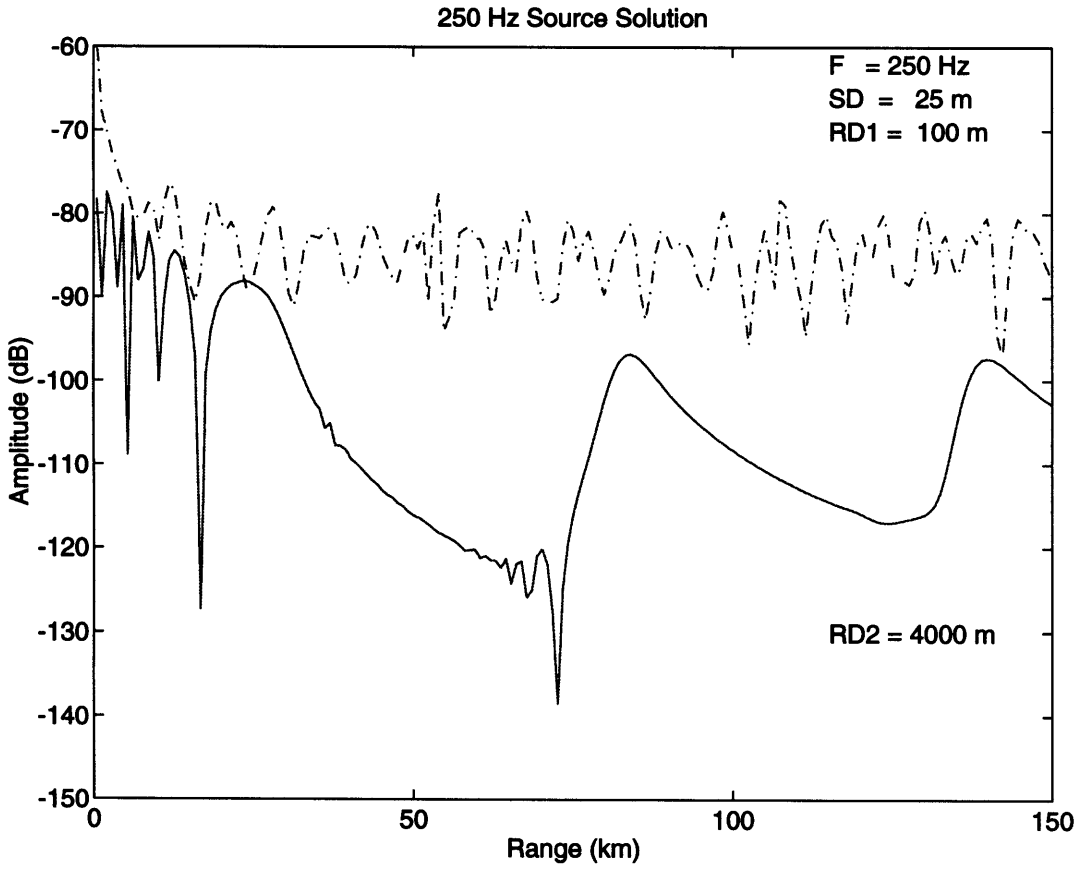

Figure 5-3: Reflectivity Result of 250 Hz Source for Test 7 Velocity Model

Chapter 6

Conclusions

A theoretical study has been carried out for a vertical array with the capability of steering the beam angle in a homogeneous ocean and in a homogeneous ocean with a free surface. A modified reflectivity technique has been implemented with the ability to calculate the total deep ocean response of a vertical array. Also, the modified code can get results with less noise, especially in the far field, which enables us to get the response as far as 55 km offset for 50 Hz sources with little noise. This enables us to study the response for different beam angles at long offsets. All of the results are compared with theoretical results. For the vertical array with different beam angles, the reflectivity results for a deep ocean response fit well with our theory for a homogeneous ocean response which assumes that the receivers are at infinite distance from the array.

The vertical array response can be divided into three components: the vertical array response without free surface, the image of the vertical array response in the homogeneous media, and the interference of the vertical array and its image array. The complex interference between the array and its image introduces the 'finger' feature into the response on the seafloor. Also, geometric spreading has a big effect on the deep ocean response. As an example, the maximum response of the vertical array with zero beam angle is vertically below the array, where it is closest to the vertical array even though the response is from the sidelobe of the beam.

The gradient has a significant effect on deep ocean responses of the vertical array.

From our study of the vertical array with 0^0, 15^0 and 30^0 beam angle, we find the response amplitudes between 25 and 30 km increased by about 6 dB, the energy is steered to that range due to the velocity gradient. This is different from the conclusion of Özlüer (1992) who applied ray tracing techniques.

It would be interesting to investigate the vertical array results of a pulse. Also, studying ray paths of each source in the array using ray tracing techniques might give us more insight into the vertical array response for the gradient ocean. Also, it is believed that different velocity gradient profiles and frequencies need future study.

Bibliography

[1] Allen, E. E., 1954, *Analytical approximations*, MTAC 8, 240-241.

[2] Braille, L. W., and Smith, R. B., 1975, *Guide to the interpretation of crustal refraction profiles*, Geophys. J. Roy. Astr. Soc., 40, 145-176.

[3] Chapman, C. H., 1978, *A new method for computing synthetic seismograms*, Geophys. J. R. Astron. Soc. 54, 481-518.

[4] Clay, C. S., and Medwin, H., 1976, *Acoustical Oceanography: principles and applications*, A Wiley-Interscience Publication.

[5] Jensen, F. B. , 1993, *PE Workshop II: Test Problem Solutions*, in PE Workshop II: Proceedings of the second parabolic workshop (NRL/BE/7181-93-0001), edited by S.A. Chin-Bing, D.B. King, J.A. Davis, and R.B. Evans (U.S. Government Printing Office, Washington, D.C.).

[6] Elliot, J. C., *Acoustic reverberation special research program initial report*, August 1991.

[7] Ewing, M., and Worzel, J. L., 1948, *Long-Range sound transmission*, in Propagation of Sound in the Ocean, Memoir 27, Geological Society of America, New York, 1948, Fig. 5, P. 19.

[8] Filon, L. N., G., 1928, *On a quadrature method for trigonometric integrals*, Proc. R. Soc. Edin. 49, 38-47.

[9] Frazer, L. N., 1978, *Synthesis of shear-coupled PL*, Ph.D. thesis, Princeton Univ.

[10] Frazer, L. N., and Gettrust, J. F., 1984, *On a generalization of Filon's method and the computation of oscillatory integrals of seismology*, Geophys. J. Roy. Astr. Soc., 76, 461-481.

[11] Frazer, L. N., 1988, *Quadrature of Wavenumber Integrals*, Seimological Algorithms, Academic Press Limited, p. 280-290.

[12] Fuchs, K., and Müller, G., 1971, *Computation of synthetic seismograms with the reflectivity method and comparison with observations*, Geophys. J. Roy. Astr. Soc., 23, 417-433.

[13] Kempner, W. C., and Gettrust, J. F., 1982a, *Ophiolites, synthetic seismograms, and ocean crustal structure 1. Comparison of ocean bottom seismometer data and synthetic seismograms for the Bay of Islands ophiolite*, J. Geophys. Res., 87, 8447-8462.

[14] Kempner, W. C., and Gettrust, J. F., 1982b, *Ophiolites, synthetic seismograms, and oceanic crustal structure 2. A comparison of synthetic seismograms of the Samail ophiolite, Oman, and ROSE refraction data from the East Pacific Rise*, J. Geophs. Res. 87, 8463-8476.

[15] Kennett, B. L. N., 1974, *Reflections, rays and reverberations*, Bull. seism. Soc. Am., 64, 1685-1696.

[16] Kennett, B. L. N., and Clarke, T. J., 1983, *Seismic waves in a stratified half-IV: P-SV save decoupling and surface wave dispersion*, Geophys. J. Roy. Astr. Soc., 72, 633-645.

[17] Kind, R., 1976, *Computation of reflection coefficients for layered media*, J. Geophys., 42, 191-200.

[18] Mallick, S., and Frazer, L. N., 1987, *Practical aspects of reflectivity modeling*, Geophysics, 52, 1355-1364.

[19] Mallick, S., and Frazer, L. N., 1988, *Rapid computation of multioffset vertical seismic profile synthetic seismograms for layered media*, Geophysics, 53, 479-491.

[20] Özlüer, Nazan Akman, *Refraction Effects on Vertical Line Array Beamforming*, thesis for Master of Science in Ocean Engineering, 1992.

[21] Robert J. Urick. *Principles of Underwater Sound.* Mc Graw Hill Book Company, Inc, New York, 1983.

[22] Smith, K. B., and Tappert, F. D., 1993, *The University of Miami Parabolic Equation Model*, MPL Technical Memorandum 432.

[23] Spudich, P., and Orcutt, J. A., 1980a, *Petrology and porosity of an oceanic crustal site: Results from waveform modeling of seismic refraction data*, J. Geophys. Res., 85, 1409-1433.

[24] Spudich, P., and Orcutt, J. A., 1980b, *A new look at the seismic velocity structure of the oceanic crust*, Rev. Geophys. Space Phys., 18, 627-645.

[25] Stephen, R. A., 1977, *Synthetic seismograms for the case of the receiver within the reflectivity zone*, Geophys. J. Roy. Astr. Soc., 51, 169-181.

[26] Tolstoy, A., Berman, D. H., and Franchi, E. R., *Ray theory versus the parabolic equation in a long-range ducted environment.* J. Acoust. Soc. Am., 78:176-189, July 1985.

[27] Olver, F. W. J., 1972, Bessel functions of integer order. *Handbook of mathematical functions* (ed. M. Abramowitz and I. A. Stegun). National Bureau of Standards.